

Enhancing GNSS Water Vapour Retrieval via Synergistic Microwave Radiometry: Thermodynamic Error Diagnosis and Bias Correction

Avinash N. Parde¹, Christina Oikonomou¹, Haris Haralambous^{1,2}

¹Frederick Research Center, Nicosia, 1036, Cyprus

²Frederick University, Nicosia, 1036, Cyprus

Correspondence: Avinash N. Parde (res.pav@frederick.ac.cy)

Abstract.

The retrieval of Precipitable Water Vapour (PWV) from Global Navigation Satellite Systems (GNSS) in thermodynamically complex environments is significantly limited by the accuracy of the weighted mean temperature (T_m). This study evaluates the efficacy of static climatological models versus dynamic ground-based microwave radiometry for T_m determination in the Eastern Mediterranean, a region characterized by sharp refractivity gradients. Using the Cyprus GNSS Meteorology Enhancement research project (CYGMEN) infrastructure in Nicosia, the performance of the ERA5-based HGPT2 model and a co-located Microwave Radiometer (MWR) was assessed against radiosonde (RS) profiles during the 2025 warm season (Spring–Summer). Diagnostic analysis reveals that the static HGPT2 model fails to resolve the diurnal thermodynamic decoupling between the boundary layer and the free troposphere, leading to a systematic overestimation of T_m exceeding 6 K during peak solar insolation. Conversely, the MWR captures short-term thermodynamic variability ($r=0.98$) but exhibits a systematic cold bias of -1.91 K in raw retrievals. It is demonstrated that a site-specific linear bias correction reduces the MWR T_m Root Mean Square Error (RMSE) from 2.32 K to 1.43 K, significantly outperforming the empirical model. Sensitivity analysis confirms that thermodynamic uncertainty dominates the error budget, outweighing uncertainties in refractivity constants by an order of magnitude. Consequently, standard climatological retrievals diverge from the synergistic MWR-GNSS method during extreme hygrometric events, introducing systematic PWV biases exceeding 1.0 mm when moisture levels surpass 45 mm. The synergistic coupling of real-time radiometric T_m with GNSS data is therefore meaningful for generating climate-quality PWV records in semi-arid coastal regions.

1 Introduction

Atmospheric water vapour (WV) is the primary greenhouse gas, contributing approximately 60 % to the natural greenhouse effect and playing a vital role in regulating the Earth's thermodynamic budget (Kiehl and Trenberth, 1997; Trenberth et al., 2005). Furthermore, WV is the main driver of latent heat transport, influencing convective systems and global precipitation patterns. High-frequency variations in Precipitable Water Vapour (PWV) correlate strongly with atmospheric instability and are a key factor in the initiation of severe weather. Specifically, rapid temporal gradients in PWV often precede heavy rainfall

32 and flash floods, acting as a reliable precursor for convective storms (Brenot et al., 2013). Consequently, assimilating high-
33 resolution PWV data into Numerical Weather Prediction (NWP) models significantly improves short-range precipitation "now-
34 casting" (Bennitt and Jupp, 2012). Accurate PWV retrieval is especially crucial for the Eastern Mediterranean, a climate change
35 "hotspot" warming faster than the global average (Giorgi, 2006; Lelieveld et al., 2012). This region is characterized by complex
36 topography and land-sea contrasts, which create sharp atmospheric refractivity gradients. The Eastern Mediterranean faces a
37 hydro-climatic paradox: a long-term drying trend (-0.5 mm/decade) alongside increasing high-intensity, short-duration flash
38 flood events (Zittis et al., 2019; Ziv et al., 2021). GNSS-derived PWV in this region exhibits strong diurnal cycles with
39 amplitudes up to 5 mm, which are closely correlated with atmospheric instability (Ziskin Ziv et al., 2020). Despite this
40 vulnerability, the Eastern Mediterranean currently lacks dense, continuous atmospheric profiling networks. Traditional
41 observation methods, such as radiosondes (RS), fail to resolve these mesoscale events due to low temporal resolution (typically
42 12-hour intervals) and significant spatial gaps (Soden and Lanzante, 1996). While satellite-based passive remote sensing offers
43 global coverage, it is often limited by revisit times, daylight dependence, or data degradation in coastal zones due to land
44 contamination in the microwave footprint (Bennartz and Bauer, 2003).

45 These limitations underscore the necessity for ground-based remote sensing techniques that offer continuous, all-weather
46 operability. Ground-based Global Navigation Satellite Systems (GNSS) meteorology has emerged as a robust technique for
47 atmospheric sounding since the seminal proposal by Bevis et al. (1992). By estimating the Zenith Total Delay (ZTD) of GNSS
48 signals traversing the neutral atmosphere, the Zenith Wet Delay (ZWD) can be isolated by subtracting the Zenith Hydrostatic
49 Delay (ZHD), which is accurately modeled from surface pressure observations (Saastamoinen, 1972). GNSS-derived PWV
50 offers significant advantages, including high temporal resolution (sub-hourly), all-weather availability, and cost-efficiency by
51 leveraging existing geodetic infrastructure (Guerova et al., 2016; Jones et al., 2020).

52 The retrieval of PWV from GNSS ZWD relies on a dimensionless conversion factor, Π , which is a function of the
53 atmospheric weighted mean temperature, T_m . Defined physically as $\int(e/T)dz/\int(e/T^2)dz$ (Askne and Nordius, 1987), T_m
54 encapsulates the thermal state of the atmospheric column. The conversion factor (Π) is nearly linearly proportional to T_m , a 1
55 K error in T_m (assuming standard atmospheric temperatures near 280 K) introduces a relative error of approximately 0.36 %
56 in the final IWV. During severe moisture events with an IWV of 50 kg m^{-2} , this translates to an absolute error of $\sim 0.18 \text{ kg m}^{-2}$.
57 Consequently, a 1 % relative error in T_m translates strictly to a 1 % relative error in IWV. Therefore, alongside the substantial
58 errors inherent in ZTD estimation—such as mapping function inaccuracies and surface pressure interpolation for the ZHD
59 (Ning et al., 2016)—the determination of T_m remains one of the primary sources of uncertainty in GNSS meteorology. In the
60 absence of in-situ profiles, T_m is commonly estimated using empirical regression models or global climatological models.
61 However, earlier studies have demonstrated that empirical T_m regressions, such as the Bevis model (Bevis et al., 1992),
62 introduce relative PWV errors of 1–2 % due to weak T_s – T_m correlations in coastal and equatorial regions, where
63 annual/semiannual variations are not adequately captured (Yao et al., 2014; Lan et al., 2016). Similarly, global grid-based T_m

64 models like GPT2w achieve RMSE <4 K at ~80 % of mid-latitude sites but degrade in data-sparse areas like the Middle East
65 and Africa, where reanalysis quality is limited (Böhm et al., 2015; Jiang et al., 2019). The Hourly Global Pressure and
66 Temperature 2 (HGPT2) model represents a major advancement by providing hourly estimates derived from ERA5 reanalysis
67 (Mateus et al., 2021). Despite recent validation of GPT2w and ECMWF models for Integrated Water Vapour (IWV) retrieval
68 in the Mediterranean (Oikonomou et al. 2018), a critical gap exists: the quantification of vertical interpolation errors in these
69 models, especially over complex coastal terrains. For instance, while recent validation studies in Cyprus demonstrate strong
70 GNSS-PWV correlations (>0.6) with ERA5 during extreme precipitation, persistent reanalysis interpolation errors are
71 highlighted in mountainous areas (Giannadaki et al., 2025). This lack of validation for HGPT2's performance in the complex
72 topography of the Eastern Mediterranean potentially exacerbates PWV biases during extreme events.

73 An alternative approach to deriving T_m is the use of ground-based Microwave Radiometers (MWR). MWRs measure
74 brightness temperatures at multiple frequencies to retrieve continuous vertical profiles of temperature and humidity. Ground-
75 based MWRs have been shown to retrieve T_m with RMSE ~1–2 K in mid-latitudes, outperforming empirical models during
76 synoptic anomalies (Cimini et al., 2010; Crewell and Löhnert, 2007; Löhnert et al., 2012). While multi-site intercomparisons
77 reveal that MWR retrievals can exhibit upper-tropospheric cold biases (up to 5 K at >2 km altitude) (Van Malderen et al.,
78 2014; Steinke et al., 2015), simple linear corrections can reduce RMSE by 20–40 % (Ning and Elgered, 2021). Operational
79 GNSS–MWR synergies for T_m bias correction have documented gains in PWV accuracy (10–30 % RMSE reduction) in
80 European networks (Vaquero-Martínez et al., 2018; Li et al., 2020). However, such applications are rare in the semi-arid
81 Eastern Mediterranean, where MWR could critically mitigate reanalysis uncertainties.

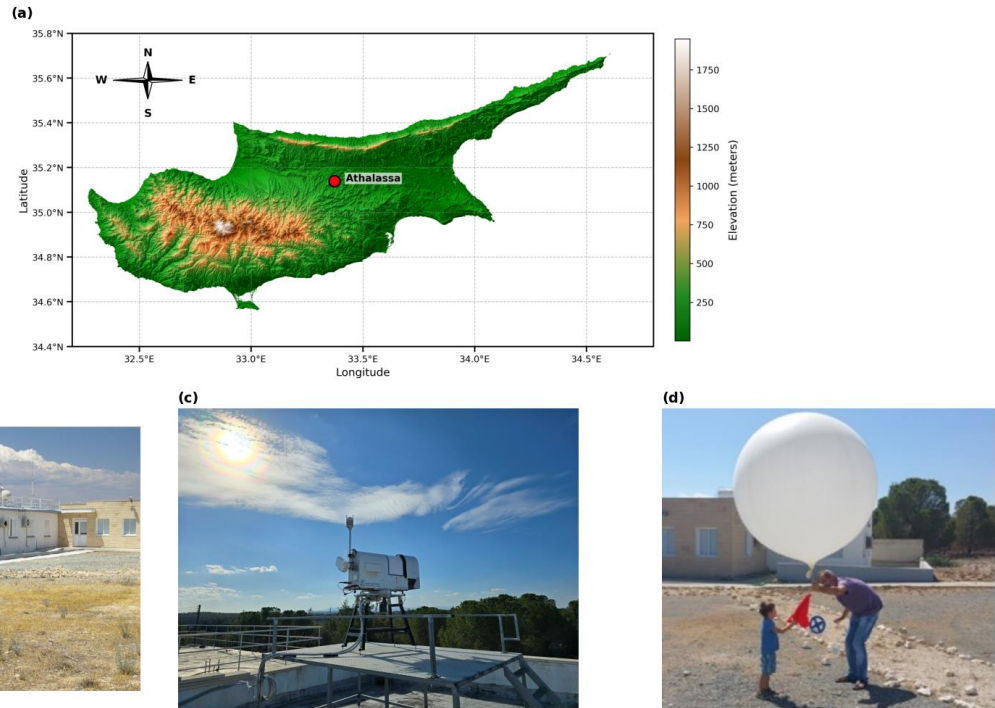
82 This study leverages the infrastructure of the CYGMEN (Cyprus GNSS Meteorology Enhancement) project, which is
83 establishing a dense, multi-sensor meteorological network in Cyprus. The network, termed CyMETEO, integrates a dense
84 array of continuous GNSS stations distributed across the island. Due to the high cost and operational complexity of radiometric
85 profiling, the network currently features a single, centralized thermodynamic 'supersite' at the Athalassa observatory, where a
86 GNSS receiver is strictly co-located with a MWR and a RS launch facility. This unique instrumental setup provides an ideal
87 testbed for inter-comparing atmospheric retrieval techniques in a coastal, semi-arid environment. The primary objective of this
88 manuscript is to evaluate the accuracy of GNSS-derived PWV over the Eastern Mediterranean by assessing the performance
89 of different T_m determination strategies. We specifically investigate the efficacy of the HGPT2 model compared to MWR-
90 derived T_m and RS benchmarks. The study aims to quantify the error budget of GNSS-PWV and determine whether the
91 inclusion of MWR data provides statistically significant improvements over the state-of-the-art HGPT2 model. The manuscript
92 is organized as follows: Section 2 describes the study area and the instrumentation of the CyMETEO network; Section 3 details
93 the methodology for GNSS processing, ZTD estimation, and the mathematical derivation of T_m from different sources; Section
94 4 presents the validation results and statistical analysis against RS reference data; and Section 5 concludes with
95 recommendations for operational PWV monitoring strategies in the region.

96

97 **2 Data and Methodology**

98 **2.1 Observational Site and CYGMEN Infrastructure**

99 The observational campaign was conducted at the Athalassa atmospheric observatory in Nicosia, Cyprus (35.15°N, 33.40°E,
100 160 m a.s.l.), situated in the central Mesaoria plain. The site is characterized by complex topography, bounded by the Troodos
101 Mountain to the southwest and the Pentadaktylos Mountain to the north, as shown in Fig. 1a. This study presents the first
102 comprehensive analysis of radiometric data acquired under the CYGMEN infrastructure project, established to monitor the
103 thermodynamic state of the Eastern Mediterranean atmosphere. To ensure robust thermodynamic profiling and validation,
104 three primary datasets were collated, as shown in Table 1:



105 **Figure 1.** Location and instrumentation at Athalassa, Cyprus. (a) Site location on the island's elevation map. (b) GNSS reference station.
106 (c) RPG-HATPRO radiometer. (d) Radiosonde balloon launching.
107

108

109 **Table 1:** Summary of Instrumentation and Datasets

Parameter	Microwave Radiometer (MWR)	Radiosonde (RS)	GNSS Station
Instrument Model	HATPRO-Gen5 (RPG)	Vaisala RS41-SGP	GNSS Receiver LEICA GR50 (Collocated)
Role in Study	Synergistic thermodynamic profiling (temperature and humidity) and IWV estimation	<i>In-situ</i> "Ground Truth" Reference	ZTD Source for PWV Retrieval

Observation Type	Passive remote sensing (22–58 GHz)	<i>In-situ</i> vertical profile (balloon-borne)	Continuous satellite signal delay
Key Variables	Brightness Temp (T_B), $T(z)$, $\rho_v(z)$, IWV	$P(z)$, $T(z)$, $RH(z)$, Geopotential Height	Zenith Total Delay (ZTD)
Vertical Range	Surface to 10 km (94 levels)	Surface to burst altitude (~30 km)	Column-integrated (single value)
Temporal Resolution	High frequency (~1 s raw, resampled to 15 min)	Periodic (launch dependent)	Continuous (high rate)
Accuracy / Noise	T_B noise < 0.11 K (K-band), < 0.32 K (V-band)	T : 0.3 K, RH : 4 % (Manufacturer spec)	ZTD precision ~mm level
Auxiliary Data	Vaisala WXT536 (Rain, Surface Met)	GPS position/height	Surface Pressure

110

111 2.2 Instrumentation and Data Processing

112 2.2.1 Microwave Radiometry (MWR)

113 The RPG-HATPRO radiometer observes downwelling atmospheric brightness temperatures (T_B) across 14 channels: seven in
114 the K-band (22–31 GHz) sensitive to water vapour, and seven in the V-band (51–58 GHz) sensitive to oxygen for temperature
115 profiling. This instrument enables the continuous retrieval of temperature (T) and absolute humidity (ρ_v) profiles on a
116 standardized grid of 94 vertical levels from the surface up to 10 km. The vertical resolution is optimized for the planetary
117 boundary layer (PBL), ranging from 10–30 m up to 500 m, and decreasing to 100–500 m in the free troposphere. For this
118 study, high-frequency MWR observations were resampled to 15-minute intervals to align with GNSS processing epochs. It is
119 a well-documented limitation of passive microwave radiometry that retrieval accuracy degrades significantly during
120 precipitation, as liquid water on the instrument's radome heavily contaminates the measured brightness temperatures (Foth et
121 al., 2024; Parde et al., 2025; Pakkattil et al., 2025; Ware et al., 2004). Because this study focused on the warm, dry season in
122 the Eastern Mediterranean (March–October 2025), rainfall events were naturally sparse. Nevertheless, to ensure data integrity,
123 real-time precipitation flags generated by the co-located Vaisala WXT536 surface weather transmitter were utilized as a strict
124 quality-control filter. Any MWR profiles retrieved during active precipitation events were excluded from the dataset to prevent
125 wet-radome anomalies from artificially skewing the thermodynamic bias analysis. To diagnose potential biases in the MWR-
126 derived T_m , the dataset was split into a training Set (April–June 2025) for regression modeling and a validation Set (July–
127 October 2025) for independent testing. In addition to thermodynamic profiling, the MWR's native retrieval algorithm possesses
128 the capacity to directly estimate IWV from its K-band brightness temperatures.

129 Any MWR profiles retrieved during active precipitation events were excluded from the dataset to prevent wet-radome
130 anomalies from artificially skewing the thermodynamic bias analysis. To mitigate T_m errors in MWR, a supervised linear

131 regression model was developed to calibrate the MWR observations. For robust independent validation, the collocated dataset
 132 was separated into two distinct temporal subsets: the training Set (April – June 2025), which was used to derive the regression
 133 coefficients, and the validation Set (July – October 2025), which was used exclusively to test the correction's performance on
 134 unseen data. A simple linear correction model was fitted to the training data using Ordinary Least Squares (OLS) minimization.
 135 The relationship is defined in Eq. (1) as:

$$136 \quad T_{m,corr} = \alpha \cdot T_{m,MWR} + \beta \quad (1)$$

137 where $T_{m,corr}$ is the corrected MWR temperature, $T_{m,MWR}$ is the raw T_m derived from the radiometer and α (slope) and β
 138 (intercept) are the learned coefficients minimizing the residual sum of squares between the MWR and RS values. Based on
 139 our training Set, the derived coefficients applied to the validation Set were $\alpha = 1.0623$ and $\beta = -15.6062$ K. In addition to
 140 thermodynamic profiling, the MWR's native retrieval algorithm possesses the capacity to directly estimate IWV from its K-
 141 band brightness temperatures.

142

143 **2.2.2 Radiosonde Data Processing**

144 To establish a rigorous validation dataset, IWV was derived from high-resolution vertical profiles obtained from collocated
 145 radiosonde launches. A strict collocation window was applied, where MWR profiles were averaged within ± 30 minutes of the
 146 balloon launch time. The raw telemetry data, comprising pressure (P), temperature, and dew point temperature (T_d), were
 147 processed to derive the total columnar water vapour content (in kg m^{-2}) through the vertical integration of specific humidity,
 148 assuming the atmosphere is in hydrostatic equilibrium. The determination of the necessary moisture variables relied on the
 149 Magnus-Tetens approximation, which provides a widely accepted empirical relationship for saturation vapour pressure. First,
 150 the actual vapour pressure (e , in hPa) was computed directly from the dew point temperature (T_d , in $^{\circ}\text{C}$). This calculation
 151 utilized the coefficients defined by Bolton (1980), which are optimized for saturation vapour pressure over liquid water in the
 152 meteorological temperature range, as shown in Eq. (2):

$$153 \quad e = 6.112 \cdot \exp\left(\frac{17.67 \cdot T_d}{T_d + 243.5}\right) \quad (2)$$

154 Subsequently, the specific humidity (q , in kg kg^{-1}) was derived via Eq. (3), representing the mass mixing ratio of water vapour
 155 to the total moist air parcel:

$$156 \quad q = \frac{\epsilon \cdot e}{P - (1 - \epsilon) \cdot e} \quad (3)$$

157 where P is the static pressure (hPa) and $\epsilon \approx 0.622$ represents the ratio of the molecular weight of water vapour to that of dry
 158 air. Once the specific humidity profile was established, the IWV was calculated by integrating q with respect to pressure. The
 159 retrieval algorithm employed the trapezoidal rule for numerical integration, which approximates the integral as the sum of
 160 discrete atmospheric layers (Eq. 4):

$$161 \quad IWV = \frac{1}{g} \sum_{i=0}^{N-1} \frac{q_i + q_{i+1}}{2} \cdot |P_{i+1} - P_i| \quad (4)$$

162 where g is the gravity dependent on altitude, $g(\phi, h)$, where ϕ represents the Geodetic latitude and h is the orthometric height.
163 P is converted to Pascals (Pa) prior to integration and N represents the total number of vertical levels in the RS profile. It
164 should be noted that IWV, representing the mass column integral in kg m^{-2} , is physically and numerically equivalent to PWV
165 expressed as a depth in millimeters (mm), assuming the standard density of liquid water (1000 kg m^{-3}). While the term IWV
166 is frequently used when discussing direct profile integration from the MWR and RS, this study uses PWV (mm) as the
167 standardized final retrieval metric to align with operational meteorological and forecasting conventions. It is important to note
168 that while the nominal manufacturer uncertainty for the Vaisala RS41 humidity sensor is stated as 4 % for individual profile
169 measurements, the uncertainty of the resulting IWV is significantly lower. Because IWV is computed by integrating hundreds
170 of discrete measurements across the vertical column (Eq. 3), uncorrelated random sensor noise is largely suppressed through
171 statistical cancellation. Consequently, the integrated variables derived from the radiosonde, such as IWV and the T_m , possess
172 the requisite precision to serve as a robust 'ground truth' standard for evaluating the finer relative uncertainties (1–2 %)
173 associated with the GNSS and MWR retrievals. To ensure a rigorous and direct intercomparison with the active MWR, the
174 radiosonde integration was strictly confined to a maximum altitude of 10 km Above Ground Level (AGL). This vertical cutoff
175 was deliberately chosen to exactly match the 10 km ceiling of the standard RPG-HATPRO retrieval grid. While GNSS
176 integrates delays through the entire atmosphere, bounding the in-situ reference data is mathematically necessary to isolate
177 profiling performance. It is well established that this 10 km threshold does not introduce a systematic dry bias when comparing
178 against total-column GNSS (Van Baelen et al., 2005). Furthermore, ambient temperatures at this altitude range from $-40 \text{ }^\circ\text{C}$
179 to $-50 \text{ }^\circ\text{C}$, strictly limiting the saturation vapour pressure. Consequently, the residual water vapour between 10 km and the
180 tropopause is thermodynamically constrained to fractions of a millimeter. Omitting this minute residual mass is functionally
181 negligible, as it falls well within the overall baseline uncertainty (typically 1–2 mm) of the total-column radiosonde IWV
182 retrieval.

183

184 **2.2.3 GNSS Data Processing**

185 ZTD estimates were derived from the collocated Leica GR50 receiver (station NICO) using the Tefnut PP software (Douša et
186 al., 2014). The processing employed a Precise Point Positioning (PPP) strategy with an elevation cutoff angle of 10° . To
187 account for tropospheric mapping errors, the Vienna Mapping Function 1 (VMF1) was applied. Station coordinates were
188 constrained to the IGS14 reference frame, and satellite orbits and clock corrections were utilized from IGS Ultra-Rapid
189 products. While IGS Final products are the gold standard for historical climate reprocessing due to their minimal orbital
190 uncertainty, this study deliberately utilized IGS Ultra-Rapid products to evaluate the proposed synergistic retrieval architecture
191 under near real-time operational constraints. Because a primary application of continuous GNSS-PWV is its assimilation into
192 short-range NWP for severe weather 'nowcasting', it is crucial to assess system performance using the satellite orbits and clocks
193 actually available during active forecasting. Although Ultra-Rapid products introduce a slight degradation in ZTD precision
194 compared to Final products, this uncertainty (typically fractions of a millimeter in PWV) remains negligible compared to the

195 massive, multi-millimeter systematic errors introduced by static thermodynamic modeling, which is the primary focus of this
 196 investigation. To isolate the ZWD, the ZHD was precisely calculated using continuous, co-located surface pressure
 197 observations obtained directly from the Vaisala WXT536 weather transmitter installed at the site, rather than relying on
 198 interpolated pressure fields. ZTD values were estimated at 15-minute intervals, directly aligning with the temporal resolution
 199 of the MWR. It must also be noted that the computation of ZHD is significantly dependent on the assumed value of the dry
 200 refractivity constant, k_1 . As established by Bevis et al. (1994) and further evaluated by Healy (2011), while k_1 is known to a
 201 high degree of relative accuracy, its residual fractional uncertainty introduces a persistent systematic bias into the ZHD
 202 estimation. Because ZWD is isolated by subtracting ZHD from the total delay, this k_1 -induced bias directly propagates into the
 203 final IWV error budget, acting alongside the conversion uncertainties analyzed later in this study.

204

205 **2.3 Thermodynamic Modeling and Synergistic Retrieval Strategy**

206 The conversion of GNSS-derived ZWD to PWV is governed by a proportionality factor, Π , whose accuracy is largely dictated
 207 by the T_m . To assess the fidelity of thermodynamic inputs for GNSS meteorology, we evaluated three distinct T_m derivation
 208 strategies. For profile-resolving instruments (MWR and RS), T_m values were computed by integrating the vertical profiles of
 209 physical temperature, $T(z)$ (K), and absolute humidity, $\rho_v(z)$ (kg m^{-3}). Consistent with Bevis et al. (1992), T_m is defined as the
 210 mean temperature of the atmosphere weighted by the water vapour partial pressure, which can be expressed in terms of vapour
 211 density as shown in Eq. (5):

$$212 \quad T_m = \frac{\int_{z_{surf}}^{z_{top}} \rho_v(z) dz}{\int_{z_{surf}}^{z_{top}} \frac{\rho_v(z)}{T(z)} dz} \quad (5)$$

213 In practice, the continuous integrals were discretized using the trapezoidal rule from the surface (z_{surf}) to the highest available
 214 profile level (z_{top}). This approach assumes linear variation of T and ρ_v between measurement levels. For standalone GNSS
 215 retrieval (where no dynamic profiles are available), T_m was derived from the HGPT2 (Hourly Global Pressure and Temperature
 216 2) model (Mateus et al., 2021). HGPT2 is an advanced 'blind' empirical model, meaning its outputs are independent of the
 217 specific observational year. While dynamic NWP models provide superior real-time meteorological data, 'blind' models like
 218 HGPT2 remain heavily utilized in standard geodetic GNSS processing where real-time meteorological or NWP data streams
 219 are unavailable. It is constructed from a comprehensive 20-year historical baseline of atmospheric data from the ERA5 global
 220 reanalysis. Unlike standard static climatologies, HGPT2 leverages the full ERA5 spatial resolution ($0.25^\circ \times 0.25^\circ$) and provides
 221 temporal resolution at 1-hour intervals for any given Day of Year (DOY). It achieves this by employing a time-segmentation
 222 concept, modeling thermodynamic variables via long-term mean values combined with annual, semi-annual, and quarterly
 223 periodic functions.

224 Applying the linear correction model (as formulated in Section 2.2.1) successfully re-centers the error distribution. To quantify

225 the benefits of sensor synergy in integrated water vapour estimation, this study defines and contrasts two distinct GNSS PWV
 226 retrieval architectures. The first, “Standard Retrieval” which is a control method utilizes the ZTD_{GNSS} combined with the T_m
 227 derived empirically from the HGPT2 climatological model (Böhm et al., 2015). Second “Synergistic Retrieval” which
 228 proposed method couples ZTD_{GNSS} with a physical T_m derived directly from a collocated MWR. For the synergistic approach,
 229 the dimensionless conversion factor (Π) was calculated dynamically using the MWR-derived T_m following Eq. (6) and Eq. (7).

$$230 \quad PWV = \Pi \cdot ZWD \quad (6)$$

$$231 \quad \Pi = \frac{10^6}{\rho_w R_v [k_2' + (k_3/T_m)]} \quad (7)$$

232
 233 where ρ_w represents the density of liquid water (1000 kg m^{-3}) and R_v is the specific gas constant for water vapour (461.52 J
 234 $\text{kg}^{-1}\text{K}^{-1}$). To assess the sensitivity of the Π to the choice of thermodynamic coefficients, three widely used formulations were
 235 employed in this study, following Davis (1985)/Thayer (1974), Bevis et al. (1994), and Rüeiger (2002), as shown in Table 2:

236 **Table 2.** Refractivity constants used in the sensitivity analysis of the Π factor, based on three commonly adopted formulations.

Method	k_2 (K hPa ⁻¹)	k_3 (K ² hPa ⁻¹)	k_2' (K hPa ⁻¹)
Davis (1985) / Thayer (1974)	64.79	3.776×10^5	16.52
Bevis et al. (1994)	70.40	3.739×10^5	22.13
Rüeiger (2002)	71.295	3.7546×10^5	22.97

237
 238 To rigorously quantify the uncertainty in the final IWV (which is numerically equivalent to PWV) retrieval and avoid
 239 fragmented error attributions, standard error propagation must be applied to the fundamental conversion Eq. 6. Assuming the
 240 uncertainties in the wet delay and the conversion factor are uncorrelated, the variance of the final IWV (σ_{IWV}^2) is expressed
 241 using partial derivatives as in Eq. (8):

$$242 \quad \sigma_{IWV}^2 = \left(\frac{\partial IWV}{\partial ZWD} \right)^2 \sigma_{ZWD}^2 + \left(\frac{\partial IWV}{\partial \Pi} \right)^2 \sigma_{\Pi}^2 \quad (8)$$

243 Evaluating these primary partial derivatives yields the proportional contributions of the geodetic and thermodynamic
 244 components as shown in Eq. (9):

$$245 \quad \sigma_{IWV}^2 = \pi^2 \sigma_{ZWD}^2 + ZWD^2 \sigma_{\Pi}^2 \quad (9)$$

246 The uncertainty in the conversion factor (σ_{Π}^2) is itself a compound term driven by the T_m and the static atmospheric refractivity
 247 constants (k_2' and k_3). Its variance is defined via partial derivatives as shown in Eq. (10):

$$248 \quad \sigma_{\Pi}^2 = \left(\frac{\partial \Pi}{\partial T_m} \right)^2 \sigma_{T_m}^2 + \left(\frac{\partial \Pi}{\partial k_2'} \right)^2 \sigma_{k_2'}^2 + \left(\frac{\partial \Pi}{\partial k_3} \right)^2 \sigma_{k_3}^2 \quad (10)$$

249 The sensitivity of the conversion factor strictly to T_m (the dynamic thermodynamic variable evaluated in this study) is quantified
 250 by its partial derivative and it represented as Eq. (11):

251

$$\frac{\partial \pi}{\partial T_m} = \pi \left[\frac{k_3}{T_m^2 \left(k_2 + \frac{k_3}{T_m} \right)} \right] \quad (11)$$

252

253

254

255

This consolidated formulation establishes the exact mathematical limits of thermodynamic error propagation. As demonstrated in the sensitivity analysis (Section 3.4), this framework accurately isolates the dynamic uncertainties driven by T_m from the baseline static biases introduced by the chosen refractivity constants.

256

2.4 Diagnostic Parameters and Error Analysis

257

258

259

260

The vertical structure of the atmosphere was analyzed by segregating the dataset into two regimes: the PBL (0-2 km), where water vapour is concentrated, and the Free Troposphere (> 2 km). Additionally, the water vapour scale height (H_v) was calculated to parameterize the vertical distribution of moisture. H_v was derived for both RS and MWR by fitting an exponential decay function (Eq. 12) to the absolute humidity profile (ρ_v).

261

$$\rho_v(z) = \rho_{v,0} \cdot \exp\left(-\frac{z}{H_v}\right) \quad (12)$$

262

263

264

265

266

267

268

269

270

271

272

273

274

275

where $\rho_v(z)$ is the absolute humidity at height z , and $\rho_{v,0}$ is the surface humidity. This curve fitting was deliberately restricted to the lowest 4 km of the atmosphere. Because this layer contains the vast majority (>90%) of the tropospheric water vapour mass, bounding the fit prevents the algorithm from heavily weighting near-zero, noisy upper-tropospheric values that mathematically degrade the fit for the boundary layer. Furthermore, the scale height metric fundamentally assumes the atmosphere conforms to a well-behaved exponential decay. Profiles yielding H_v values outside the physically realistic range of 0.1 to 4.0 km were excluded from the statistical analysis to prevent artificial statistical skewing during complex meteorological states (e.g., deep convective mixing) where the underlying exponential model is invalid. Forcing a mathematical fit onto these non-exponential profiles yields physically meaningless artifacts. Therefore, a Quality Assurance filter was applied, bounding the analysis to the physically realistic range of $0.1 \text{ km} < H_v < 4.0 \text{ km}$. Profiles yielding values outside this range were discarded because they indicate the underlying exponential model itself is invalid for that specific atmospheric profile, preventing artificial statistical skewing in the instrument intercomparison. Profiles yielding H_v values outside the physically realistic range of 0.1 to 4.0 km were excluded from the statistical analysis. To evaluate the performance limitations of standard climatological models under varying hygrometric conditions, the systematic error (ΔPWV) was defined as the residual between the synergistic and standard approaches (Eq. 13):

276

$$\Delta PWV = PWV_{Synergistic} - PWV_{Standard} \quad (13)$$

277

278

279

280

The dataset was stratified into discrete bins of 5 mm PWV to isolate regimes of moisture abundance. Within each bin, the mean bias and $\pm 1\sigma$ uncertainty were computed. These statistics were utilized to determine the "Systematic Bias Threshold," defined herein as the specific hygrometric threshold where the systematic model error exceeds 1 mm. Finally, the propagation of thermodynamic uncertainty into the moisture retrieval was quantified via linear regression analysis. This compared the

281 relative error in T_m (HGPT2 vs. MWR) against the resulting relative error in PWV, serving as an empirical verification of the
282 theoretical sensitivity approximation given in Eq. (14):

$$283 \quad \frac{\Delta PWV}{PWV} \approx \frac{\Delta T_m}{T_m} \quad (14)$$

284 **3 Results**

286 The following evaluation follows a top-down diagnostic approach. First, the macroscopic baseline performance of the final
287 derived moisture products is established. Subsequently, the underlying thermodynamic variables driving these discrepancies
288 are isolated, culminating in the development of a targeted calibration scheme to mitigate the identified biases.

289 **3.1 Temperature and Humidity Profile Validation**

290 MWR-retrieved temperature T and ρ_v profiles were validated against collocated RS observations at 00:00 UTC and 12:00 UTC
291 during March–October 2025. Profiles were stratified into the planetary boundary layer (PBL; 0–2 km) and free troposphere
292 (>2 km), as shown in Figs. 2 and 3. Mean vertical temperature profiles show agreement between MWR and RS (Fig. 2a–b).
293 In the boundary layer (0–2 km), MWR retrieves temperature with high precision ($r > 0.98$, $RMSE < 1.5$ K). Above 2 km, a cold
294 bias is observed in the MWR retrieval, reaching -5.16 K at 12 UTC (Fig. 2f). Despite this bias, the linearity remains strong
295 ($r \approx 0.97$), indicating the sensor captures relative thermal variations aloft despite the absolute offset. This confirms the trend
296 observed in the mean profiles, where the MWR underestimates temperatures in the mid-to-upper troposphere. Consequently,
297 the RMSE increases substantially to approximately 6.4 – 6.7 °C. The stark contrast in accuracy between the lower and upper
298 troposphere is a known characteristic of ground-based microwave radiometry (Parde et al., 2025; Pakkattil et al., 2025). The
299 high accuracy below 2 km is attributed to the high information content of the opaque V-band channels (51–58 GHz), whose
300 weighting functions peak near the surface. Above 2 km, these weighting functions broaden significantly, reducing vertical
301 resolution and causing a "smearing" effect where the instrument provides a volume-averaged temperature rather than a precise
302 point measurement. The observed cold bias is likely a result of the retrieval algorithm (e.g., neural network) relying heavily
303 on a climatological *a priori* dataset that does not perfectly represent the thermal conditions of the transition season observed,
304 or systematic offsets in the radiative transfer model (absorption coefficients) used for training.

305 The mean ρ_v profiles (Figs. 3a–b) show the expected exponential decrease of moisture with height. At 00 UTC, the profiles
306 align reasonably well. However, at 12 UTC, the MWR profile exhibits a structural deviation between 1–2 km, failing to capture
307 the smooth moisture gradient recorded by the RS. This discrepancy may be attributed to the MWR's limited vertical resolution
308 during periods of active daytime mixing or complex humidity layering. The retrieval of humidity in the lower atmosphere
309 shows moderate agreement but is less accurate than the temperature retrievals. Performance is notably better at night (00 UTC)
310 with r of 0.878 and RMSE of 1.98 g m⁻³. At 12 UTC, the correlation drops to 0.744, and the scatter increases (RMSE = 2.31 g
311 m⁻³). A negative bias persists at both times (-0.51 g m⁻³ at 00 UTC and -0.91 g m⁻³ at 12 UTC), indicating a tendency for the

312 MWR to underestimate moisture content in the boundary layer, particularly during the day. Surprisingly, the statistical linearity
313 for ρ_v improves slightly or remains stable above 2 km, likely due to the lower overall magnitude of humidity at these heights.
314 The correlation coefficients remain stable (~ 0.87). In contrast to the lower levels, the bias shifts to slightly positive values
315 (0.23 g m^{-3} at 00 UTC and 0.46 g m^{-3} at 12 UTC), suggesting a slight moist bias in the MWR retrievals aloft. The linear fits
316 (Figs. 3e–f) align closely with the 1:1 line, with slopes near unity (0.90 and 1.00), indicating that the MWR effectively captures
317 the free tropospheric humidity trends despite the lower absolute values. The difficulty in retrieving accurate ρ_v profiles,
318 particularly at 12 UTC, stems from the limited vertical resolution of the K-band channels (22–31 GHz). Unlike temperature
319 profiling, humidity profiling offers very few independent degrees of freedom (typically <3), making it difficult for the MWR
320 to resolve sharp vertical gradients often present at the top of the convective boundary layer during the daytime. The structural
321 deviation and underestimation are common issues linked to the "smoothing" error inherent in passive radiometry, where sharp
322 moisture inversions are averaged out. Furthermore, the persistent bias suggests potential uncertainties in the water vapour
323 absorption models (spectroscopic parameters) or non-representative training data used in the retrieval algorithm.

324

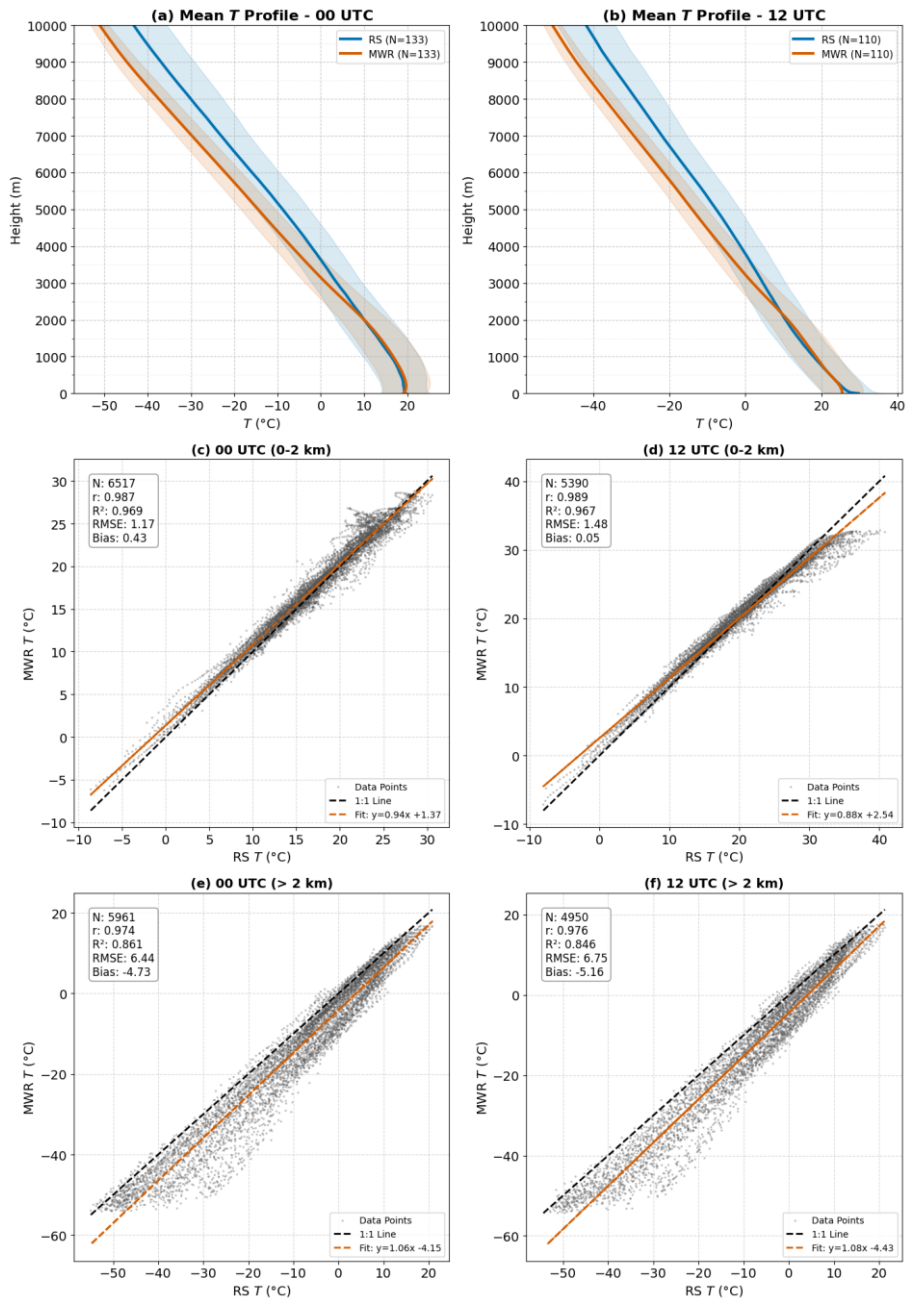
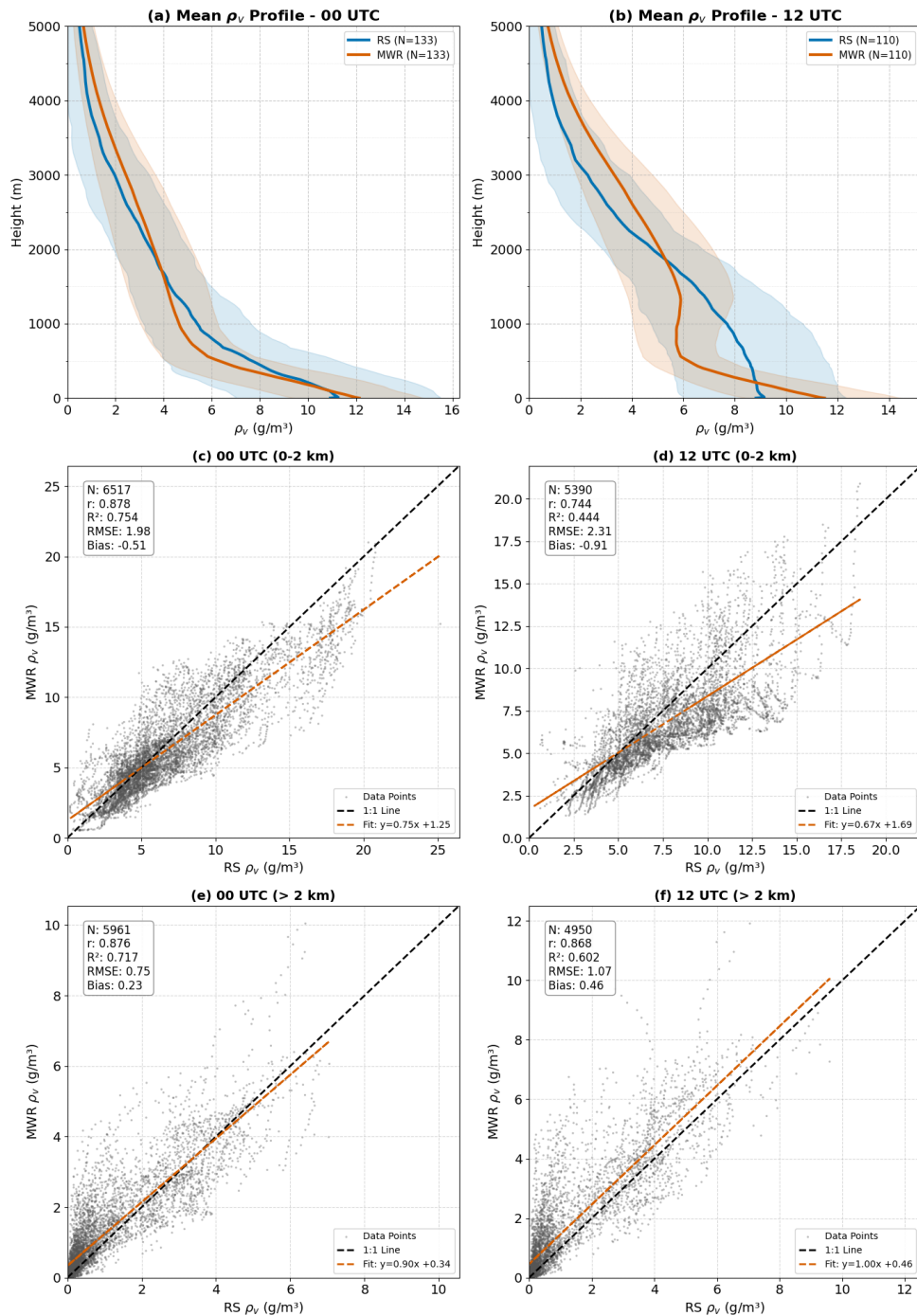


Figure 2. Comparison of radiosonde and microwave radiometer (MWR) temperature profiles: (a–b) Mean vertical temperature (T) profiles at 00 and 12 UTC with variability shading; (c–f) Scatter comparisons for the lower (0–2 km) and upper (>2 km) atmosphere at both times.

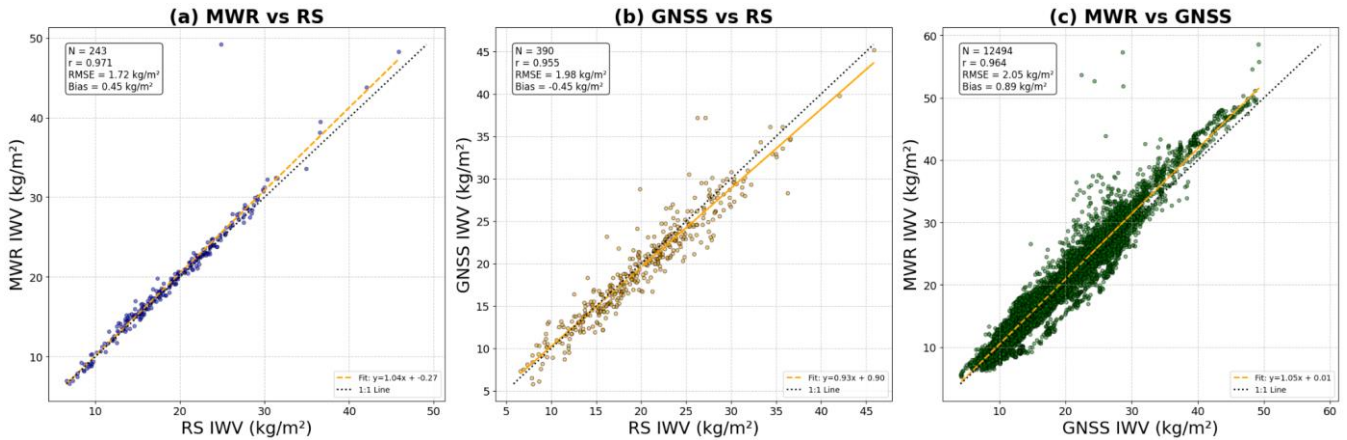
325
326
327
328



329 **Figure 3.** Comparison of radiosonde and microwave radiometer (MWR) absolute humidity (ρ_v) profiles: (a–b) Mean vertical ρ_v profiles at
 330 00 and 12 UTC with variability shading; (c–f) Scatter comparisons for the lower (0–2 km) and upper (>2 km) atmosphere at both times.
 331
 332

333 **3.2 Integrated Water Vapour (IWV) and Scale Height (H_v) Validation**

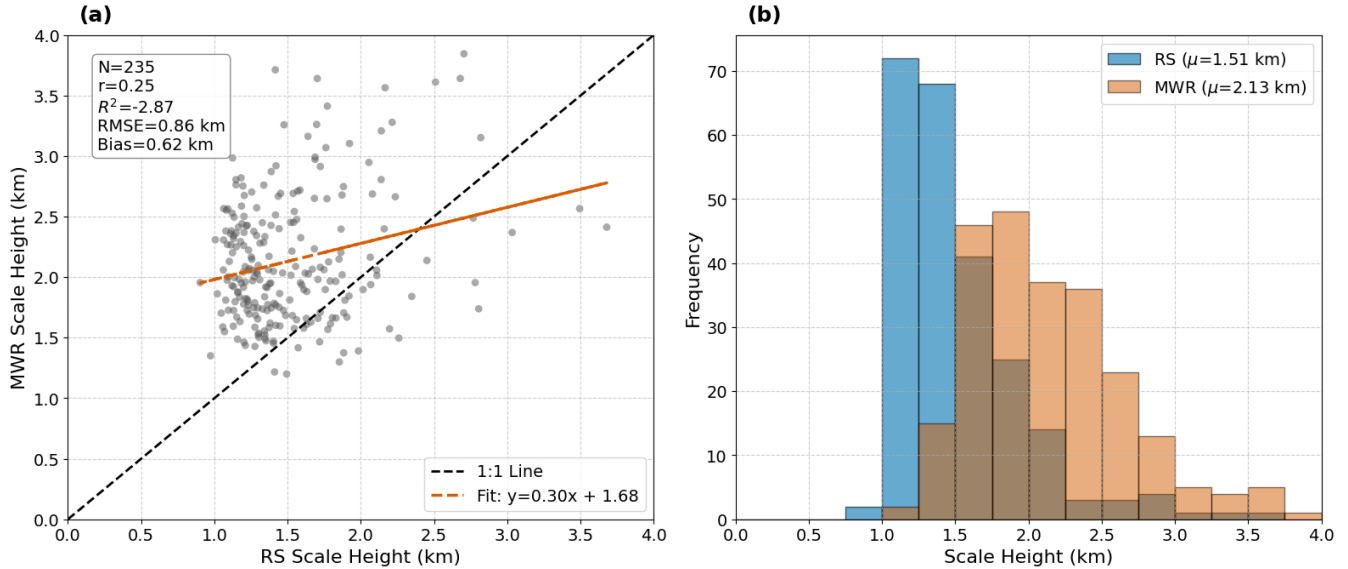
334 Unlike vertical profiling, the MWR excels in measuring total column quantities. The comparison with RS yields an excellent
 335 correlation ($r=0.971$) and a low RMSE of 1.72 kg m^{-2} . This performance disparity—superior IWV versus degraded profiles—
 336 confirms that while the sensor cannot resolve vertical structural details due to smoothing error, the radiometric brightness
 337 temperature in the K-band remains strictly proportional to the total precipitable water mass. The GNSS-derived IWV shows a
 338 slight negative bias relative to RS (-0.45 kg m^{-2}), whereas it relative to the MWR exhibits a positive bias ($+0.45 \text{ kg m}^{-2}$). The
 339 cumulative offset observed in the MWR-GNSS intercomparison ($+0.89 \text{ kg m}^{-2}$) highlights the systematic differences in
 340 calibration and retrieval assumptions between active (GNSS) and passive (MWR) techniques. The GNSS underestimation is
 341 likely driven by errors in the T_m derived from the static HGPT2 model, a hypothesis further explored in Section 3.4. To further
 342 diagnose the structural limitations of the retrievals, we evaluated the water vapour H_v . While H_v is admittedly a single-
 343 parameter representation of the complex atmospheric moisture profile, it is a crucial parameter that provides a representative
 344 value for the rate at which water vapour decreases with altitude—a key factor in understanding atmospheric stability, cloud
 345 formation, and radiative transfer processes. In this study, it is utilized specifically as a diagnostic metric to quantify the vertical
 346 structural limitations of passive microwave remote sensing. The comparison of H_v calculated from RS and MWR profiles is
 347 shown in Fig. 5. Unlike the high-fidelity IWV retrievals, the MWR-derived scale height shows negligible correlation with RS
 348 observations ($r=0.25$, $R^2=-2.87$) and a massive systematic positive bias of 0.62 km . The histograms (Fig. 5b) further elucidate
 349 this discrepancy: while the RS scale heights follow a narrow, physically realistic distribution centered around a mean (μ) of
 350 1.51 km , the MWR distribution is artificially broad and shifted to significantly higher values ($\mu=2.13 \text{ km}$).



351 **Figure 4.** Intercomparison of integrated water vapour (IWV) retrieved from Microwave Radiometer (MWR), GNSS, and Radiosonde
 352 observations. (a) MWR IWV versus radiosonde IWV, (b) GNSS IWV (derived using HGPT2 T_m) versus radiosonde IWV, and (c) MWR
 353 IWV versus GNSS IWV (derived using HGPT2 T_m).
 354

355 The large scatter and ambiguity in the MWR estimates—which completely dwarf the individual least-squares fit
 356 uncertainties of the exponential regression—are a direct consequence of the instrument's physical limitations. H_v is highly
 357 sensitive to the sharp vertical gradient of humidity at the top of the planetary boundary layer. However, the K-band channels
 358 (22–31 GHz) utilized for humidity profiling possess broad weighting functions, restricting the vertical degrees of freedom to

359 typically fewer than three. Because the MWR lacks the vertical resolution to capture sharp moisture inversions, the retrieval
 360 algorithm mathematically smears the moisture mass upward. This inherent 'smoothing error' artificially elongates the vertical
 361 moisture profile, effectively inflating the calculated e-folding depth. Therefore, the inclusion of this H_v analysis serves to
 362 transparently demonstrate a critical operational boundary: while the MWR is an excellent standard for IWV, it is significantly
 363 unreliable and mathematically unsuited for characterizing vertical moisture compactness. The significant deviations observed
 364 in these macroscopic retrieval products necessitate a deeper investigation into the intermediate thermodynamic variables
 365 driving the conversion process. Consequently, the isolated performance of the T_m is evaluated in Section 3.3, followed by the
 366 introduction of a post-retrieval MWR calibration scheme in Section 3.4 designed to mitigate these native biases.



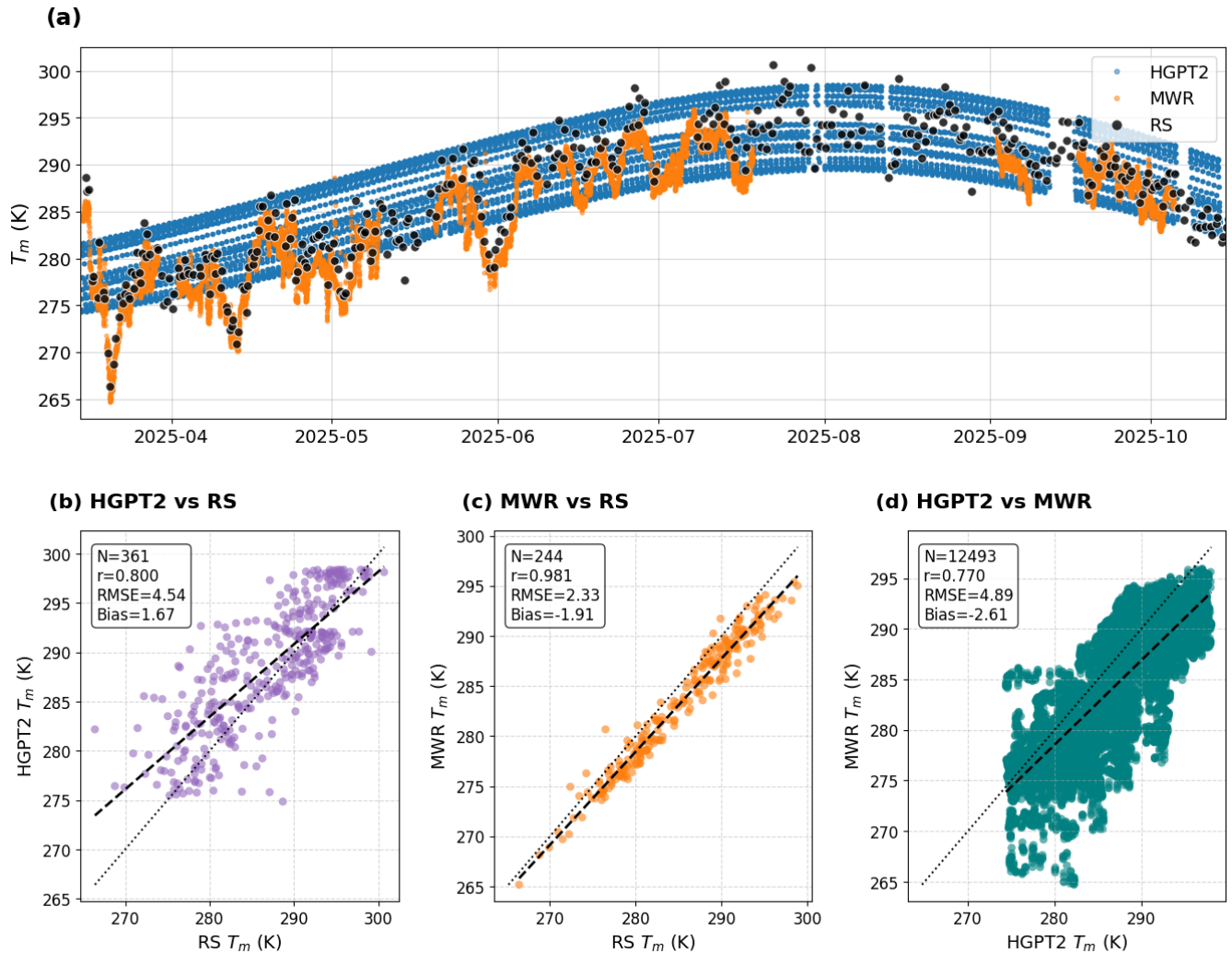
367 **Figure 5:** Comparison of scale height from radiosonde (RS) and microwave radiometer (MWR): (a) Scatter plot with 1:1 line and linear fit,
 368 including summary statistics; (b) Frequency distributions showing mean scale heights for RS and MWR.
 369

370

371 3.3 Weighted Mean Temperature (T_m) Validation

372 The accurate estimation of the T_m is critical for converting GNSS-derived ZWD into PWV. The performance of T_m derived
 373 from the MWR and the empirical GPT2w model (HGPT2) was evaluated against RS measurements, which serve as the "ground
 374 truth." The results are presented in Fig. 6. The time series (Fig. 6a) illustrates the seasonal evolution of T_m from April to October
 375 2025. The Radiosonde observations (black dots) show significant variability, capturing synoptic-scale weather fluctuations.
 376 The MWR-derived T_m (orange dots) tracks these fluctuations with remarkable precision, overlaying the RS points almost
 377 perfectly. In stark contrast, the HGPT2 model (blue dots) provides a smooth, climatological curve. While it captures the general
 378 seasonal trend, it completely misses the day-to-day thermodynamic variability, often overestimating T_m during cooler transient
 379 events and underestimating it during warmer anomalies. The empirical model shows only moderate performance ($r=0.800$)
 380 with a substantial spread ($RMSE = 4.54$ K). A systematic positive bias of 1.67 K indicates that HGPT2 generally overestimates

381 the atmospheric temperature profile in this region. The scatter plot reveals a diffuse, "cloud-like" distribution, confirming its
382 inability to capture real-time atmospheric dynamics. The MWR demonstrates superior performance, achieving a near-perfect
383 correlation ($r=0.981$). The RMSE is significantly reduced to 2.33 K, which is nearly half the error of the empirical model.
384 Interestingly, the MWR exhibits a negative bias of -1.91 K, suggesting a systematic underestimation of T_m . Crucially, this bias
385 does not originate in the free troposphere, but rather in the planetary boundary layer (0–3 km). Since T_m is weighted by water
386 vapour pressure, this "cold bias" indicates the MWR is underestimating the intense near-surface heating or the sharp lapse
387 rates characteristic of the Nicosia environment. Despite this offset, the tight linearity indicates that MWR is an excellent source
388 for capturing real-time T_m variations. Comparing the large dataset of MWR against HGPT2 ($N=12,493$) confirms the
389 discrepancy between dynamic and static modeling. The correlation is lower ($r=0.770$) and the scatter is large (RMSE = 4.89
390 K), further proving that static empirical models are insufficient for high-precision GNSS meteorology compared to dynamic
391 radiometer measurements. While errors in ZTD estimation contribute significantly to the overall uncertainty budget, the
392 specific error introduced during the conversion from delay to water vapour is linearly dependent on the accuracy of T_m .
393 Assuming a given ZTD, a standard rule of thumb states that a 1 % relative error in T_m translates to roughly a 1 % relative error
394 in the resulting PWV. By switching from a static model (HGPT2, ~ 4.5 K error) to a dynamic sensor (MWR, ~ 2.3 K error),
395 the uncertainty in the GNSS water vapour product is effectively halved. This validates the "synergistic" approach of using
396 collocated MWR thermal data to process GNSS signals.



397
 398 **Figure 6.** Comparison of weighted mean temperature (T_m) derived from HGPT2, MWR, and Radiosonde (RS) during March–November
 399 2025. (a) Time series of T_m estimates from all three sources. (b–d) Scatter plots showing statistical comparisons between: (b) HGPT2 vs.
 400 RS, (c) MWR vs. RS, and (d) HGPT2 vs. MWR.

401

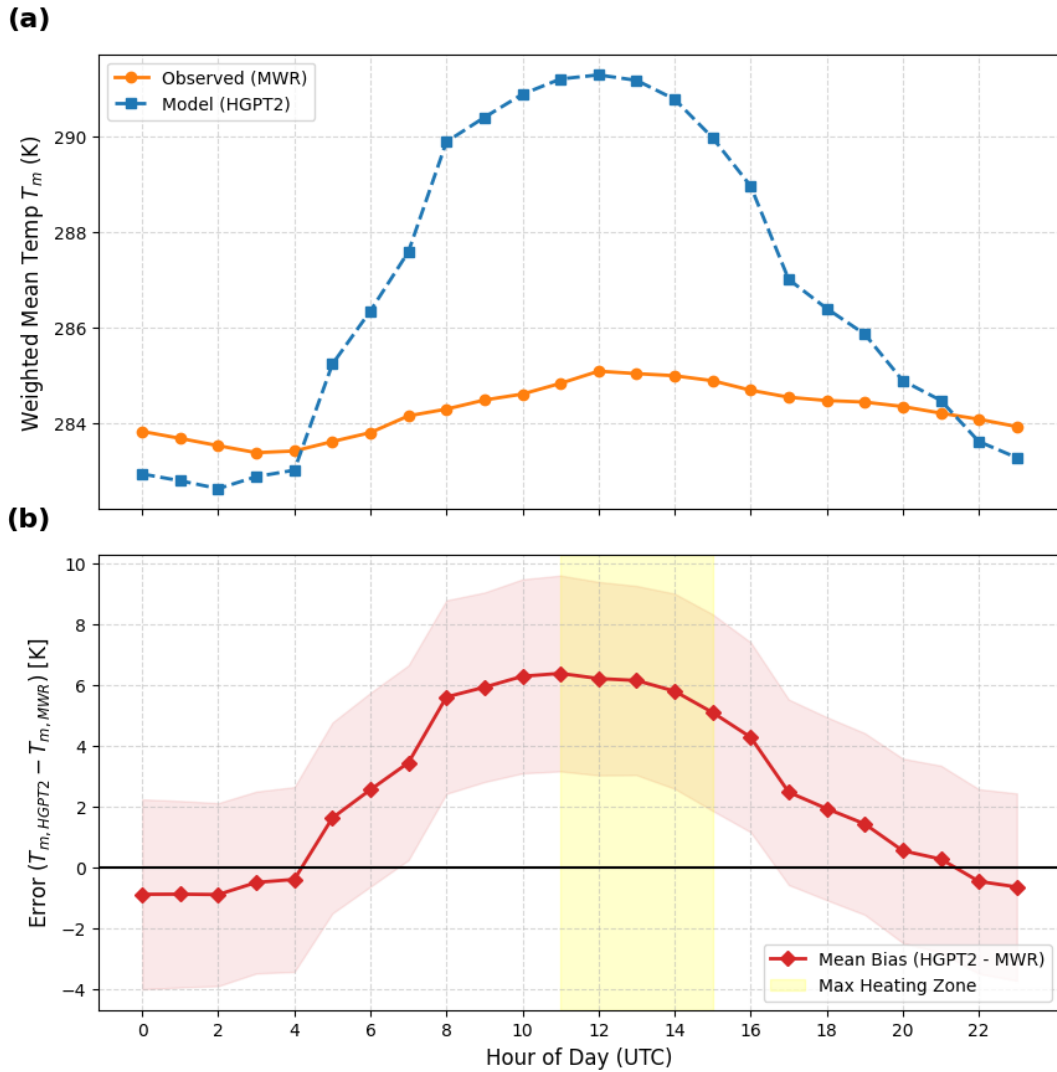
402 3.4 Diagnostic Analysis of Thermodynamic Conversion Uncertainty

403 3.4.1 Diurnal Bias Amplification in Static Models

404 To pinpoint the physical origin of the HGPT2 model's deficiency, a diurnal cycle analysis was performed (Fig. 7). While the
 405 previous statistical metrics indicated a general positive bias, the temporal breakdown in Fig. 7a reveals that this error is not
 406 uniform, but is driven by a fundamental misrepresentation of atmospheric thermodynamics. The MWR-derived T_m (orange
 407 line) exhibits a physically realistic, dampened diurnal amplitude of approximately 1.5 K. This stability reflects the high thermal

408 inertia of the tropospheric column, which does not heat rapidly in response to surface insolation. In stark contrast, the HGPT2
409 model (blue line) displays an exaggerated diurnal wave with an amplitude exceeding 8.5 K, peaking synchronously with solar
410 noon (12:00 UTC). As previously documented in the literature (Wang, 2005; Bock, 2021), deriving T_m via empirical regression
411 on surface temperature (T_s) is known to introduce spurious diurnal cycles. Our observations confirm this intrinsic limitation:
412 because the empirical model's periodic functions are overly sensitive to T_s , it assumes intense surface-level heating propagates
413 uniformly through the column, failing to capture the true thermodynamic decoupling between the turbulent planetary boundary
414 layer and the stable free troposphere. During the hours of peak solar insolation (11:00–14:00 UTC), the coastal environment
415 experiences active convective mixing and the onset of the sea breeze, which dramatically alters the vertical distribution of
416 water vapour. If the underlying reanalysis climatology fails to adequately resolve the sharp moisture capping inversion at the
417 top of the daytime planetary boundary layer (PBL), it will misrepresent the T_m weighting function. Specifically, if the model
418 traps too much moisture near the intensely heated surface—or fails to capture the thermodynamic decoupling between the
419 turbulent PBL and the stable free troposphere — the integral will disproportionately weight the hottest atmospheric layers.
420 This coupled temperature-humidity mechanism physically manifests as the severe diurnal bias peak effect observed in Fig. 7b,
421 where the systematic bias surges to over +6 K. This demonstrates that high-precision GNSS meteorology requires synergistic
422 MWR data to capture both the true thermal stability and the dynamic vertical moisture weighting of the atmosphere.

423



424
425
426
427
428

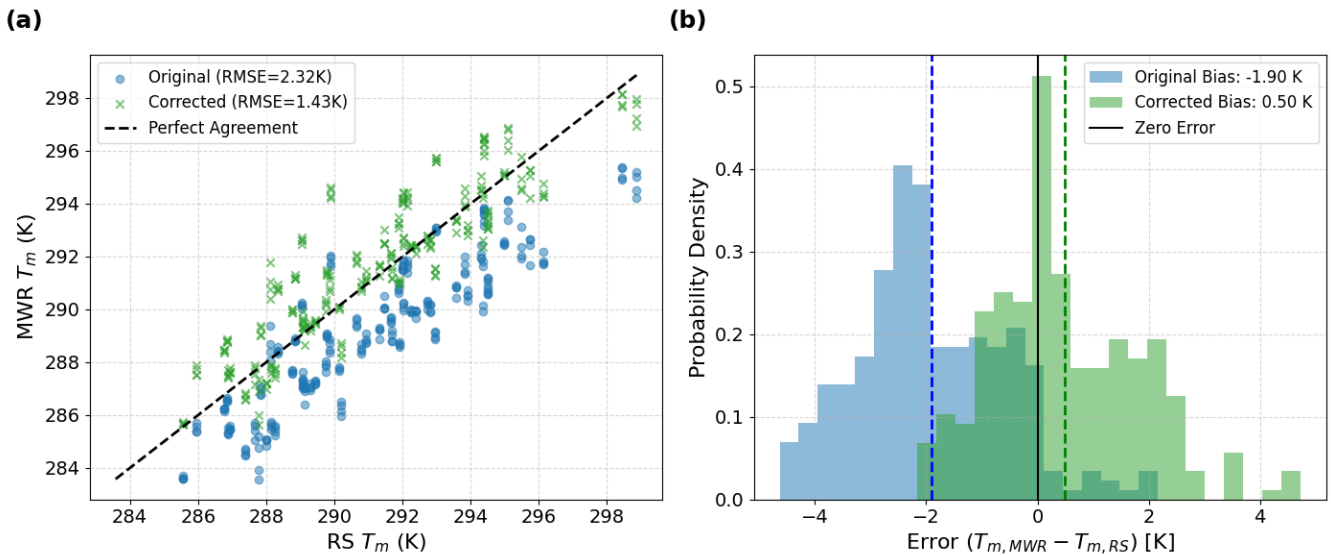
Figure 7. Diurnal variation of weighted mean atmospheric temperature T_m derived from microwave radiometer (MWR) observations and HGPT2 model simulations (top panel). The bottom panel shows the corresponding hourly mean bias ($T_{m,HGPT2} - T_{m,MWR}$), with shaded envelopes indicating variability. The yellow shaded region highlights the period of maximum daytime heating.

429 3.4.2 Calibration and Bias Correction of MWR T_m

430 Fig. 8 presents a statistical validation of the MWR derived T_m against co-located RS observations. The analysis highlights the
431 necessity and efficacy of a linear bias correction scheme to improve GNSS-PWV conversion accuracy. The scatter plot (Fig.
432 2a) reveals a distinct systematic deviation in the original MWR retrieval relative to the RS reference. The data points
433 consistently fall below the 1:1 identity line, indicating a negative bias in the raw MWR T_m product. The original RMSE is 2.32
434 K. This error is largely driven by the systematic offset rather than random scatter, as evidenced by the high linearity (R^2) of

435 the relationship. The thermodynamic profiles were retrieved using the manufacturer's standard Neural Network (NN)
 436 algorithm, trained on Region historical RS data.

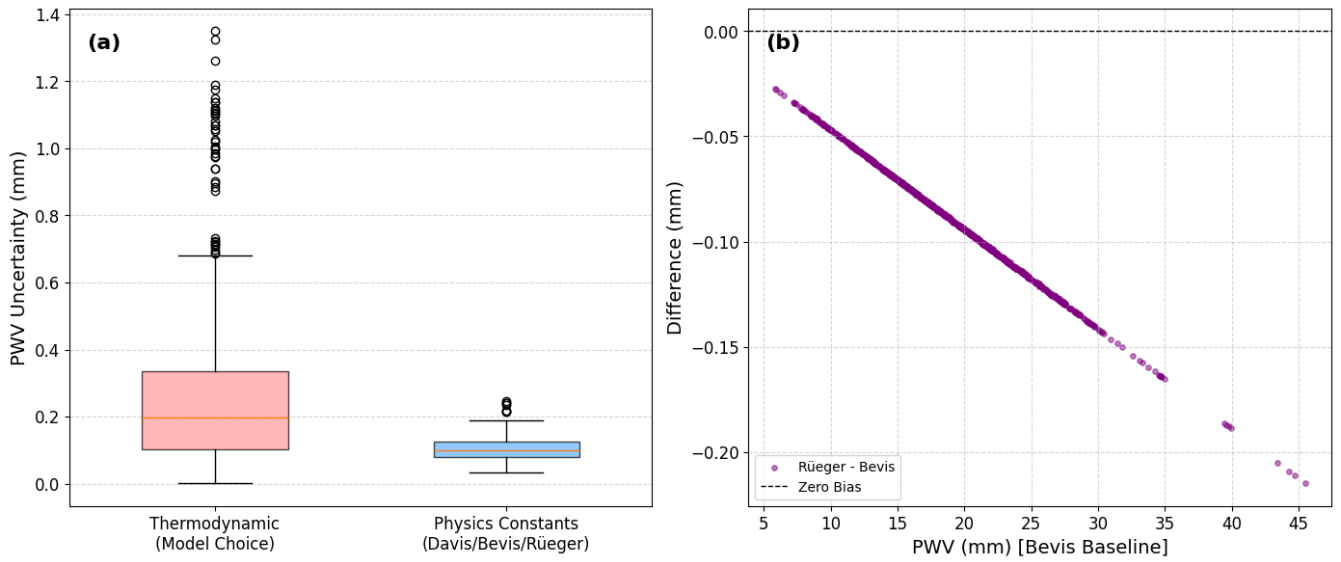
437 The Probability Density Function (PDF) of the errors ($T_{m,MWR} - T_{m,RS}$) in Fig. 8b clearly visualizes the bias shift. The pre-
 438 correction distribution is non-Gaussian and shifted significantly to the negative domain, with a mean bias (μ) of -1.90 K. In
 439 the context of GNSS meteorology, a T_m error of ≈ 2 K translates to a relative PWV error of approximately 0.7–1.0 %. For
 440 climate monitoring, this represents a significant systematic dry bias. Applying the linear correction model (as formulated in
 441 Section 2.2.1) successfully re-centers the error distribution. The post-correction bias is reduced to 0.50 K, and the histogram
 442 aligns symmetrically around the zero-error line. The correction reduces the RMSE to 1.43 K, which is consistent with the
 443 theoretical accuracy limit of ground-based radiometric profiling (typically 1–2 K). The remaining spread (width of the green
 444 histogram) represents the random error component, likely attributable to instrumental noise and the imperfect spatiotemporal
 445 matching between the instantaneous MWR zenith view and the drifting radiosonde balloon. The correction methodology
 446 effectively removes the systematic instrumental bias without artificially compressing the natural variability of the atmosphere.
 447 The reduction of RMSE by ~ 38 % (from 2.32 K to 1.43 K) confirms that site-specific calibration of T_m is a mandatory
 448 processing step for generating climate-quality GNSS-PWV datasets.



449 **Figure 8.** Evaluation of weighted mean temperature T_m correction against Radiosonde (RS) observations. (a) scatter plots of original and
 450 bias-corrected MWR-derived T_m versus RS T_m , with the dashed line indicating perfect agreement. (b) presents the probability density of
 451 errors ($T_{m,MWR} - T_{m,RS}$) before and after correction, demonstrating a substantial reduction in cold bias and RMSE.
 452
 453

454 3.4.3 Uncertainty Budget Analysis

455



456 **Figure 9.** (a) PWV uncertainty attributed to thermodynamic assumptions and to the choice of refractivity constants. (b) Difference in GNSS-
 457 derived PWV resulting from the use of alternative refractivity constant formulations relative to Bevis et al. (1994).
 458

459
 460 In standard GNSS network processing, the largest source of PWV uncertainty is often the interpolation or modeling of
 461 surface pressure required to calculate the ZHD (Van Malderen et al., 2022). However, the CYGMEN observatory setup
 462 mitigates this spatial interpolation error by utilizing the co-located Vaisala WXT536 sensor, which has a stated pressure
 463 accuracy of ± 0.5 hPa. A 0.5 hPa pressure uncertainty propagates to approximately 1.15 mm of error in the ZHD. After applying
 464 the Π conversion factor, this restricts the pressure-induced PWV uncertainty to roughly ± 0.17 mm. Because this high-precision
 465 localized pressure data effectively minimizes ZHD uncertainty, the accuracy of the T_m parameterization emerges as the
 466 dominant remaining variable in the PWV error budget for this site.

467 It is important to note that the complete error budget for GNSS-derived PWV encompasses significant uncertainties
 468 originating from the ZTD estimation phase itself. These include geodetic errors such as satellite orbit and clock uncertainties,
 469 mapping function inaccuracies, and site-dependent electromagnetic effects like signal scattering and multipath. While these
 470 geodetic factors are critical, the following component-wise uncertainty analysis (Fig. 9) specifically isolates the errors
 471 introduced during the subsequent conversion step (Π). To decouple these retrieval contributions, two primary sources of
 472 uncertainty were isolated: the thermodynamic parameterization of T_m and the selection of atmospheric refractivity constants
 473 (k_2' , k_3). When decoupling these retrieval contributions, it is critical to distinguish between the statistical nature of the
 474 underlying error sources. As demonstrated by Healy (2011), uncertainties in the atmospheric refractivity constants (k_2' , k_3) act
 475 strictly as static systematic biases; selecting a different set of published constants permanently shifts the baseline of the Π by
 476 a fixed margin. Conversely, the uncertainty originating from the T_m parameterization is a dynamic, compound error. As
 477 highlighted by Wang et al. (2005) and Bock et al. (2021), empirical T_m models derived from surface temperatures often fail to

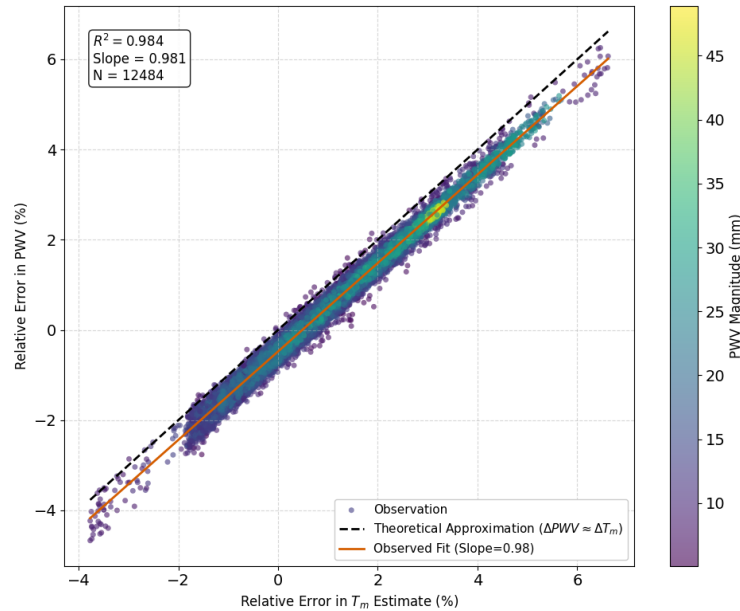
478 capture the true profile variance, introducing both a systematic bias (the model's mean regional offset) and a substantial random
479 error component (the statistical scatter, or RMSE, driven by real-time thermodynamic variability and diurnal decoupling).
480 While Fig. 9 juxtaposes these two distinct sources to illustrate their relative bounding magnitude on the final IWV product,
481 their significantly different statistical behaviors—static bias versus dynamic scatter—must be acknowledged. As illustrated in
482 Fig. 9(a), and explicitly evaluating the components of the conversion uncertainty framework established in Eq. (10), the
483 variance introduced by the T_m estimation strategy ($\sigma_{T_m}^2$) significantly outweighs the influence of the physical constants
484 ($\sigma_{k_2}^2, \sigma_{k_3}^2$). Feeding our empirically derived thermodynamic uncertainties into the partial derivative formulation defined in Eq.
485 (11) specifically, substituting the HGPT2 RMSE of 4.54 K versus the corrected MWR RMSE of 1.43 K as our σ_{T_m} values—
486 yields an isolated PWV retrieval error of approximately 1-2 mm due to stochastic thermodynamic variability. In contrast,
487 evaluating the exact mathematical limits of the refractivity coefficients ($\sigma_{k_2}, \sigma_{k_3}$) defined here as the maximum divergence
488 between the historical Davis et al. (1985), the standard Bevis et al. (1994), and the updated Rüeiger (2002) formulations—
489 results in an uncertainty an order of magnitude smaller. Fig. 9(b) further resolves the impact of the refractivity constants,
490 showing the differential bias between the oldest (Davis) and newest (Rüeiger) standards. The relationship is linear and
491 proportional to the total water vapour content, consistent with a scaling of the Π factor. While the transition to the Rüeiger
492 (2002) constants introduces a systematic positive shift, the magnitude of this correction (typically <0.2 mm for standard
493 loading) is negligible for synoptic meteorological applications compared to the noise induced by T_m errors. However, for long-
494 term climatological trend analysis where stability is paramount, consistent adherence to the Rüeiger (2002) standard is
495 recommended to eliminate this small, but persistent systematic bias. Overall, the correction of the T_m is 2.5 times more
496 important than selection of the constant.

497

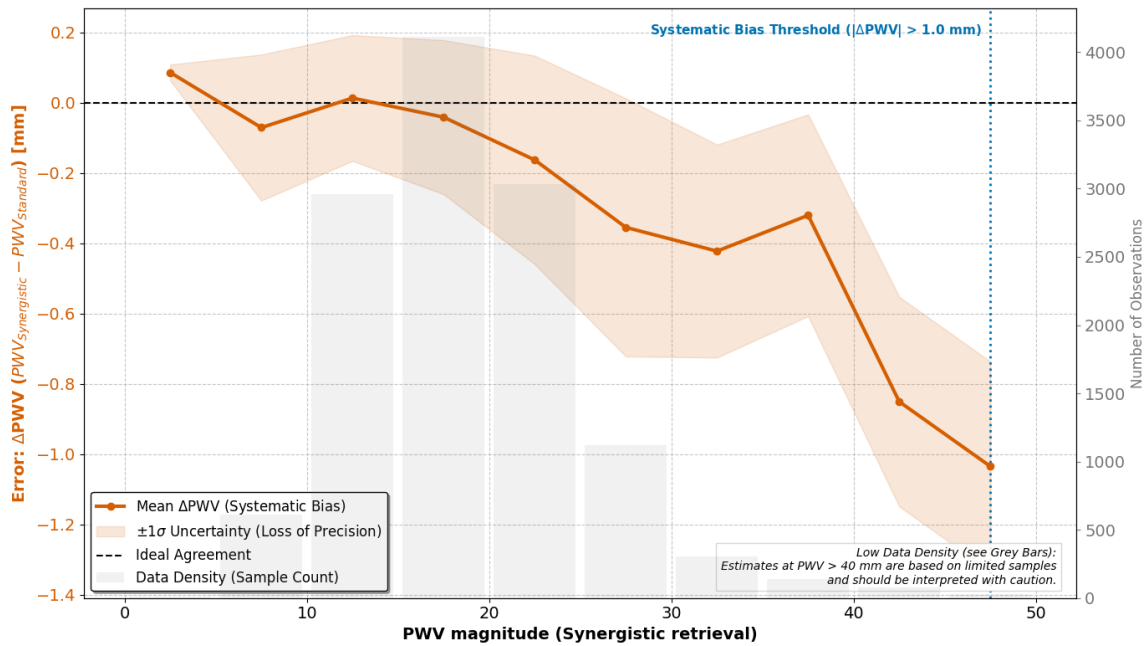
498 3.5 Error Propagation and Synergistic Retrieval Assessment

499 In this section, the PWV was derived using bias-corrected mean temperature (T_m) and constant values based on the study by
500 Rüeiger (2002), as mentioned in the Sect. 3.4. The impact of T_m errors on the final PWV product was analyzed to quantify the
501 benefits of the synergistic retrieval method. Fig. 10 visualizes the direct relationship between the relative error in T_m and the
502 resulting relative error in PWV. The plot reveals a strictly linear relationship ($R^2=0.984$) with a slope of 0.981. This confirms
503 the theoretical approximation that $(\Delta PWV/PWV) \approx (\Delta T_m/T_m)$. The color gradient indicates that this linear error propagation
504 holds true across all PWV magnitudes (from <10 mm to >45 mm). This implies that temperature errors propagate directly into
505 moisture errors regardless of the humidity level, making accurate T_m crucial at all times. Fig. 11 investigates the systematic
506 difference (ΔPWV) between the synergistic retrieval (using MWR T_m) and a standard retrieval (using empirical T_m) as a function
507 of moisture abundance (PWV magnitude). For drier conditions (PWV < 25 mm), the difference is minimal (near zero), and
508 the uncertainty (shaded region) is low. This suggests that for low humidity, the choice of T_m source is less critical. As
509 atmospheric moisture increases (> 25 mm), a significant negative bias emerges. The curve dips sharply, reaching nearly -1.0

510 mm at extreme humidity (45+ mm). The 'Systematic Bias Threshold' marker indicates that beyond 45 mm, the discrepancy
 511 exceeds 1.0 mm. The fact that the bias magnitude scales directly with total PWV provides physical confirmation that the error
 512 source is located in the boundary layer, where the bulk of the water vapour resides. The growing negative bias demonstrates
 513 that standard GNSS processing (using static models like HGPT2) systematically overestimates water vapour during extreme
 514 events compared to the more accurate synergistic method. Rather than extrapolating these localized errors to regional
 515 hydrological impacts, we emphasize the primary empirical observation: the systemic deviation of the standard empirical model
 516 scales proportionally with the magnitude of the PWV regime. Crucially, this systematic overestimation of moisture during
 517 extreme events is deeply intertwined with the diurnal cycle of the local atmosphere. This analysis quantifies the specific
 518 operational penalty of utilizing static climatological models in this region, demonstrating that HGPT2 incurs an IWV error
 519 exceeding 1.0 kg m^{-2} during severe thermodynamic events. As previously established (Fig. 7), the static HGPT2 model
 520 displays an exaggerated diurnal wave with an amplitude exceeding 8.5 K. Because the static model fails to account for the
 521 thermodynamic decoupling between the heated boundary layer and the cooler free troposphere during the day, this T_m error
 522 artificially inflates the amplitude of the GNSS-derived PWV diurnal cycle during peak solar insolation. By utilizing the
 523 synergistic retrieval approach, this spurious daytime moisture amplification is effectively mitigated. While further multi-site,
 524 long-term studies are required to assess the broader impacts on regional operational forecasting, our localized dataset clearly
 525 indicates that integrating real-time MWR thermal data successfully removes diurnal artifacts and reduces systematic
 526 measurement biases at this site.



527 **Figure 10.** Driver of model failure: Impact of weighted mean temperature (T_m) accuracy on PWV retrieval.
 528
 529
 530



531 **Figure 11.** Systematic breakdown and instability of the Standard GNSS model under extreme thermodynamic conditions.
 532
 533

534 **4 Discussions**

535 The results of this study necessitate a fundamental re-evaluation of how T_m parameterization errors are parameterized in GNSS
 536 meteorology, particularly within thermodynamically complex, semi-arid coastal environments like the Eastern Mediterranean.
 537 The pronounced failure of the static HGPT2 model to capture the diurnal T_m cycle reveals a structural limitation inherent to
 538 empirical modeling. The observed "diurnal bias peak" effect is not merely a statistical anomaly; it represents a physical
 539 disconnect. Static empirical models rely heavily on T_s , effectively assuming that intense surface-level heating propagates
 540 uniformly through the atmospheric column. This assumption critically breaks down during the daytime in the EM, where the
 541 turbulent planetary boundary layer (PBL) aggressively decouples from the stable free troposphere. Evidence for this severe
 542 decoupling is explicitly documented in the high-vertical-resolution RS profiles collected during the campaign. Because the
 543 passive MWR struggles to effectively capture this sharp boundary—a direct result of the broad weighting functions and
 544 degraded vertical resolution inherent to its K-band observations—the instrument exhibits a 'smoothing error' across the
 545 inversion layer. This structural limitation highlights exactly why applying a site-specific bias correction to the MWR's native
 546 output is a necessary prerequisite for precision GNSS meteorology. Furthermore, the failure of the reanalysis climatology to
 547 properly resolve the sharp moisture capping inversion during the onset of the daytime sea-breeze significantly corrupts the
 548 moisture-weighted T_m integral. Ground-based microwave radiometry overcomes this structural blindness by directly measuring
 549 the integrated thermal emissions of the column.

550 However, the performance of the MWR in this study highlights the duality of passive microwave remote sensing: it is highly
551 proficient at retrieving integral quantities but degrades severely when resolving differential or gradient-based parameters. The
552 successful reduction of the T_m RMSE via site-specific linear correction confirms that the MWR's K-band and V-band channels
553 effectively capture the true thermal inertia of the troposphere. The initial systematic cold bias observed aloft is a known artifact
554 of ill-posed neural network retrievals (Cimini et al., 2006; Löhnert and Maier, 2012). Because the vertical resolution of passive
555 microwave observations degrades rapidly with height, the retrievals become heavily constrained by historical training datasets
556 (the climatological prior), which often fail to capture localized, transition-season lapse rates in the free troposphere.
557 Conversely, the complete failure of the MWR to derive a physically realistic water vapour scale height (H_v) exposes the
558 "smoothing error" inherent to passive radiometry. Because the broad weighting functions of the K-band channels cannot
559 resolve sharp boundary layer moisture inversions, the retrieval algorithm mathematically smears the moisture mass upward.
560 This confirms that while MWR serves as a robust standard for total column mass, researchers must exercise extreme caution
561 when utilizing its smoothed profiles to characterize vertical moisture compactness.

562 While this study relies on a single-site, multi-month dataset, the physical mechanisms identified have broad relevance beyond
563 the Nicosia region. The Eastern Mediterranean serves as a highly representative climatic hotspot for semi-arid coastal
564 environments experiencing enhanced warming and intensified hydrological cycles. It is important to note that the specific
565 threshold of >45 mm identified here is characteristic of the climatological moisture capacity of the Eastern Mediterranean
566 during extreme summer anomalies. While the exact numerical value of this 'Systematic Bias Threshold' will vary
567 geographically depending on local atmospheric dynamics and latitude, the underlying physical principle remains universal:
568 empirical T_m models systematically degrade proportionally to the total atmospheric moisture mass during severe local
569 extremes. The core vulnerability exposed in this research—that static global models are structurally blind to sharp boundary
570 layer thermodynamic decoupling during peak insolation—is a fundamental physics problem, not a local anomaly. Therefore,
571 the proposed synergistic MWR-GNSS retrieval architecture provides a universally applicable solution for mitigating
572 systematic dry biases in any complex terrain or coastal environment globally. While the simple linear regression applied in
573 this study proved highly effective at correcting systematic T_m biases for operational GNSS conversions, there remains room
574 for algorithmic improvement. As the CYGMEN infrastructure accumulates a multi-year climatological database of high-
575 resolution radiosonde profiles, future work should focus on complementary Neural Network (NN) training. By retraining the
576 MWR retrieval algorithms using site-specific radiative transfer modeling rather than relying on the manufacturer's regional
577 historical priors, the native temperature and humidity profiles can be further optimized at the retrieval level.

578 Finally, our component-wise uncertainty analysis clarifies the error propagation chain in the GNSS-PWV conversion
579 process, shifting the paradigm of where optimization efforts should be focused. Historically, significant effort within the
580 geodetic community has been expended on refining atmospheric refractivity constants. However, we demonstrate that the error
581 induced by transitioning from the historical Davis et al. (1985) formulations to the modern Rüeiger (2002) constants is

582 practically negligible (<0.2 mm) for synoptic meteorological applications. The true "weak link" in the retrieval chain is
583 unequivocally the thermodynamic parameterization, which introduces errors an order of magnitude larger.

584

585 **5 Conclusion**

586 This study demonstrated that the accuracy of GNSS-derived Precipitable Water Vapour (PWV) in the Eastern Mediterranean
587 region, is significantly affected by the thermodynamic rigidity of static climatological models. By implementing a synergistic
588 retrieval strategy that couples GNSS delays with real-time ground-based microwave radiometry (MWR), we successfully
589 quantified and mitigated these limitations. The investigation yielded three primary methodological conclusions. First, we
590 established that standard empirical models (e.g., HGPT2) are structurally incapable of resolving the diurnal thermodynamic
591 decoupling between the boundary layer and free troposphere. This deficiency leads to severe systematic errors (the "diurnal
592 bias peak" effect) exceeding 6 K in weighted mean temperature (T_m) during peak solar insolation, which directly propagates
593 into a PWV bias >1.0 mm during extreme hygrometric events. Second, the MWR proved to be a superior source for T_m
594 parameterization errors, provided that site-specific calibration is applied. The development of a linear bias correction scheme
595 reduced the MWR T_m root-mean-square error from 2.32 K to 1.43 K. This correction substantially reduces the conversion-
596 related uncertainty in the GNSS water vapour product compared to standard climatological approaches. Third, the component-
597 wise sensitivity analysis confirmed that thermodynamic parameterization is a highly significant source of uncertainty that
598 exacerbates existing geodetic ZTD errors, outweighing uncertainties in refractive index constants by an order of magnitude.
599 Consequently, the proposed combined retrieval represents a highly valuable architectural upgrade for monitoring severe
600 weather in complex coastal environments like the Eastern Mediterranean. However, it must be acknowledged that there are
601 many sites worldwide where the deployment of microwave radiometers may not be justified. Given the high capital and
602 operational costs of radiometric hardware, the presence of other unmitigated geodetic uncertainties, and the adequate
603 performance of static T_m models in less thermodynamically complex regions, this synergistic approach is best reserved for
604 targeted deployments in highly vulnerable climatic hotspots.

605 For the climate-sensitive Eastern Mediterranean region, relying on static models for GNSS processing risks systematically
606 masking moisture trends during heatwaves and deep convection. We therefore recommend the operational integration of
607 collocated MWR observations into national GNSS processing chains. Where collocation is not feasible, future work should
608 focus on assimilating MWR-derived diurnal shape functions into static models to bridge the gap between climatology and
609 reality. This study establishes the "Corrected Synergistic Method" as a robust benchmark for generation of climate-quality
610 water vapour datasets in complex thermodynamic environments.

611

612 **Data availability**

613 The MWR and GNSS data used in this study are available from the CYGMEN project archive upon request. High resolution
614 Radiosonde data available from the Department of Meteorology (DoM), Cyprus. The ERA5 reanalysis data can be downloaded
615 from the Copernicus Climate Change Service (C3S) Climate Data Store.

616

617 **Author contributions**

618 ANP carried out the GNSS, MWR, and Radiosonde data processing, performed the synergistic PWV retrievals and error
619 diagnosis, and wrote the initial version of the paper. CO and HH conceptualized the study, acquired the funding and resources
620 for the CYGMEN infrastructure, and supervised the investigation. All authors discussed the results, edited, and proofread the
621 paper.

622

623 **Competing interests**

624 All authors declare that they have no conflict of interest.

625

626 **Acknowledgements**

627 We would like to express our sincere gratitude to the Cyprus Department of Meteorology (DoM) and in particular to Physicist
628 and Meteorology Officer Dr. Demetris Charalambous, for his invaluable guidance and for providing access to essential
629 resources at Athalassa observatory in Nicosia, Cyprus.

630

631 **Financial support**

632 The present study is funded by the Strategic Infrastructure project CYGMEN, which is implemented in the frames of Cohesion
633 Policy Programme “THALIA 2021-2027” and is co-funded by the European Union.

634

635 **References**

636 Askne, J. and Nordius, H.: Estimation of tropospheric delay for microwaves from surface weather data, *Radio Sci.*, 22, 379–
637 386, <https://doi.org/10.1029/RS0221003p00379>, 1987.

638 Bennartz, R. and Bauer, P.: Sensitivity of microwave radiances at 85–183 GHz to precipitating ice particles, *Radio Sci.*, 38,
639 8075, <https://doi.org/10.1029/2002RS002626>, 2003.

640 Bennett, G. V. and Jupp, A.: Operational assimilation of GPS zenith total delay observations into the Met Office numerical
641 weather prediction models, *Mon. Weather Rev.*, 140, 2706–2719, <https://doi.org/10.1175/MWR-D-11-00156.1>, 2012.

642 Bevis, M., Businger, S., Herring, T. A., Rocken, C., Anthes, R. A., and Ware, R. H.: GPS meteorology: Remote sensing of
643 atmospheric water vapor using the Global Positioning System, *J. Geophys. Res.*, 97, 15787–15801,
644 <https://doi.org/10.1029/92JD01517>, 1992.

645 Bevis, M., Businger, S., Chiswell, S., Herring, T. A., Anthes, R. A., Rocken, C., and Ware, R. H.: GPS meteorology: Mapping
646 zenith wet delays onto precipitable water, *J. Appl. Meteorol.*, 33, 379–386, [https://doi.org/10.1175/1520-0450\(1994\)033<0379:GMMZWD>2.0.CO;2](https://doi.org/10.1175/1520-0450(1994)033<0379:GMMZWD>2.0.CO;2), 1994.

648 Böhm, J., Möller, G., Schindelegger, M., Pain, G., and Weber, R.: Development of an improved empirical model for slant
649 delays in the troposphere (GPT2w), *GPS Solut.*, 19, 433–441, <https://doi.org/10.1007/s10291-014-0403-7>, 2015.

650 Bolton, D.: The computation of equivalent potential temperature, *Mon. Weather Rev.*, 108, 1046–1053,
651 [https://doi.org/10.1175/1520-0493\(1980\)108<1046:TCOEPT>2.0.CO;2](https://doi.org/10.1175/1520-0493(1980)108<1046:TCOEPT>2.0.CO;2) 1980.

652 Brenot, H., Neméghaire, J., Delobbe, L., Clerbaux, N., De Meutter, P., Deckmyn, A., Delcloo, A., Frappez, L., and Van
653 Roozendael, M.: Preliminary signs of the initiation of deep convection by GNSS, *Atmos. Chem. Phys.*, 13, 5425–5449,
654 <https://doi.org/10.5194/acp-13-5425-2013>, 2013.

655 Bock, O., Bosser, P., Flamant, C., Doerflinger, E., Jansen, F., Fages, R., Bony, S. and Schnitt, S.: Integrated water vapour
656 observations in the Caribbean arc from a network of ground-based GNSS receivers during EUREC 4 A. *Earth System Science*
657 *Data*, 13(5), pp.2407-2436. <https://doi.org/10.5194/essd-13-2407-2021>. 2021.

658 Cimini, D., Westwater, E. R., Gasiewski, A. J., Klein, M., Leuski, V. Y., and Dowlathshahi, S.: Thermodynamic atmospheric
659 profiling during the 2010 Winter Olympics using ground-based microwave radiometry, *IEEE T. Geosci. Remote*, 49, 4959–
660 4969, <https://doi.org/10.1109/TGRS.2011.2154337>, 2011.

661 Cimini, Domenico, Tim J. Hewison, Lorenz Martin, Jürgen Güldner, Catherine Gaffard, and Frank S. Marzano. "Temperature
662 and humidity profile retrievals from ground-based microwave radiometers during TUC." *Meteorologische Zeitschrift* 15, no.
663 1: 45-56. 2006.

664 Crewell, S. and Löhnert, U.: Accuracy of boundary layer temperature profiles retrieved with multifrequency multiangle
665 microwave radiometry, *IEEE T. Geosci. Remote*, 45, 2195–2201, doi: 10.1109/TGRS.2006.888434. 2007.

- 666 Douša, J. and Václavovic, P.: Real-time zenith tropospheric delays in support of numerical weather prediction applications,
667 *Adv. Space Res.*, 53, 1347–1358, <https://doi.org/10.1016/j.asr.2014.02.021>, 2014.
- 668 Davis, J. L., Herring, T. A., Shapiro, I. I., Rogers, A. E. E., and Elgered, G.: Geodesy by radio interferometry: Effects of
669 atmospheric modeling errors on estimates of baseline length, *Radio Sci.*, 20, 1593–1607,
670 <https://doi.org/10.1029/RS020i006p01593>, 1985.
- 671 Foth, A., Lochmann, M., Saavedra Garfias, P. and Kalesse-Los, H.: Determination of low-level temperature profiles from
672 microwave radiometer observations during rain. *Atmospheric Measurement Techniques*, 17(24), pp.7169-7181, 2024.
- 673 Gaffen, D. J.: Temporal inhomogeneities in radiosonde temperature records, *J. Geophys. Res.*, 99, 3667–3676,
674 <https://doi.org/10.1029/93JD03179>, 1994.
- 675 Giannadaki, D., Oikonomou, C., Haralambous, H., Tymvios, F., and Loizou, E.: Validation of precipitable water vapour
676 products using CyMETEO GNSS network in Cyprus, in: Eleventh International Conference on Remote Sensing and
677 Geoinformation of the Environment (RSCy2025), Vol. 13816, 397–409, SPIE, 2025.
- 678 Giorgi, F.: Climate change hot-spots, *Geophys. Res. Lett.*, 33, L08707, <https://doi.org/10.1029/2006GL025734>, 2006
- 679 Guerova, G., Jones, J., Douša, J., Dick, G., de Haan, S., Pottiaux, E., Bock, O., Pacione, R., Elgered, G., Vedel, H., and Bender,
680 M.: Review of the state of the art and future prospects of the ground-based GNSS meteorology in Europe, *Atmos. Meas. Tech.*,
681 9, 5385–5406, <https://doi.org/10.5194/amt-9-5385-2016>, 2016.
- 682 Held, I. M. and Soden, B. J.: Robust responses of the hydrological cycle to global warming, *J. Climate*, 19, 5686–5699,
683 <https://doi.org/10.1175/JCLI3990.1>, 2006.
- 684 Healy, S.B.: Refractivity coefficients used in the assimilation of GPS radio occultation measurements. *Journal of Geophysical*
685 *Research: Atmospheres*, 116(D1). <https://doi.org/10.1029/2010JD014013>. 2011.
- 686 Jiang, P., Ye, S., Chen, D., Liu, Y., and Xia, P.: Development of time-varying global gridded Ts-Tm model for precise GPS-
687 PWV retrieval, *Atmos. Meas. Tech.*, 12, 1233–1249, <https://doi.org/10.5194/amt-12-1233-2019>, 2019.
- 688 Jones, J., Guerova, G., Douša, J., Dick, G., de Haan, S., Pottiaux, E., Bock, O., Pacione, R., Elgered, G., Vedel, H., and Bender,
689 M.: Advanced GNSS Tropospheric Products for Monitoring Severe Weather Events and Climate, Springer, Cham,
690 <https://doi.org/10.1007/978-3-030-13901-8>, 2020.
- 691 Kiehl, J. T. and Trenberth, K. E.: Earth's annual global mean energy budget, *B. Am. Meteorol. Soc.*, 78, 197–208,
692 [https://doi.org/10.1175/1520-0477\(1997\)078<0197:EAGMEB>2.0.CO;2](https://doi.org/10.1175/1520-0477(1997)078<0197:EAGMEB>2.0.CO;2), 1997.

693 Lan, Z., Zhang, B., and Geng, T.: Establishment and analysis of global gridded Tm-Ts relationship model, *Geodesy and*
694 *Geodynamics*, 7, 101–107, <https://doi.org/10.1016/j.geog.2016.02.001>, 2016.

695 Lelieveld, J., Hadjinicolaou, P., Kostopoulou, E., Chenoweth, J., El Maayar, M., Giannakopoulos, C., Hannides, C., Lange,
696 M. A., Tanarhte, M., Tyrlis, E., and Xoplaki, E.: Climate change and impacts in the Eastern Mediterranean and the Middle
697 East, *Climatic Change*, 114, 667–687, <https://doi.org/10.1007/s10584-012-0418-4>, 2012.

698 Li, H., Wang, X., Wu, S., Zhang, K., Chen, X., Qiu, C., Zhang, Q., and Li, L.: Development of an improved model for
699 prediction of short-term heavy precipitation based on GNSS-derived PWV, *Remote Sens.*, 12, 4101,
700 <https://doi.org/10.3390/rs12244101>, 2020.

701 Löhnert, U. and Maier, O.: Operational profiling of temperature using ground-based microwave radiometry at Payerne:
702 Prospects and challenges, *Atmos. Meas. Tech.*, 5, 1121–1134, <https://doi.org/10.5194/amt-5-1121-2012>, 2012.

703 Mateus, P., Mendes, V. B., and Plecha, S. M.: HGPT2: an ERA5-based global model to estimate relative humidity, *Remote*
704 *Sens.*, 13, 2179, <https://doi.org/10.3390/rs13112179>, 2021.

705 Ning, T. and Elgered, G.: Intercomparison of MAX-DOAS vertical profile retrieval algorithms: studies on field data from the
706 CINDI-2 campaign, *Atmos. Meas. Tech.*, 14, 1–35, <https://doi.org/10.5194/amt-14-1-2021>, 2021.

707 Ning, Tong, J. Wang, G. Elgered, G. Dick, J. Wickert, Markus Bradke, M. Sommer, R. Querel, and D. Smale. "The uncertainty
708 of the atmospheric integrated water vapour estimated from GNSS observations." *Atmospheric Measurement Techniques* 9, no.
709 1. 79-92. doi:10.5194/amt-9-79-2016. 2016.

710 Pakkattil, A., Parde, A. N., Wagh, S., Lonkar, P., and Ghude, S. D.: Wintertime Intercomparison of Specific Humidity and
711 Temperature Profiles Measured by Microwave Radiometer (MWR), Radiosonde, and INSAT-3DR Sounder Over Delhi, India,
712 *J. Geophys. Res. Atmos.*, 130, e2025JD044462, <https://doi.org/10.1029/2025JD044462>, 2025.

713 Parde, A. N., Ghude, S. D., Prasad, V. S., Hari Prasad, K. B. R. R., Dhangar, N. G., Lonkar, P., and Rajeevan, M.: Influence
714 of ground-based microwave radiometer profile assimilation on fog genesis forecasts in the winter boundary layer of Northern
715 India, *J. Geophys. Res. Atmos.*, 130, e2024JD042224, <https://doi.org/10.1029/2024JD042224>, 2025.

716 Oikonomou, C., Tymvios, F., Pikridas, C., Bitharis, S., Balidakis, K., Michaelides, S., ... and Charalambous, D.: Tropospheric
717 delay performance for GNSS integrated water vapor estimation by using GPT2w model, ECMWF's IFS operational model and
718 in situ meteorological data, *Adv. Geosci.*, 45, 363–375, <https://doi.org/10.5194/adgeo-45-363-2018>, 2018.

719 Realini, E., Gatti, A., Reguzzoni, M., Sampietro, D., and Venuti, G.: GNSS-based precipitable water vapor retrieval for severe
720 weather monitoring: The 2014 Genoa flood case study, *Adv. Space Res.*, 53, 1–10, <https://doi.org/10.1016/j.asr.2014.02.015>,
721 2014.

722 Rüeiger, J. M.: Refractive index formulae for radio waves, in: Proceedings of the FIG XXII International Congress,
723 Washington, D.C., USA, 19–26 April 2002, 1–13, 2002.

724 Ross, R. J. and Elliott, W. P.: Tropospheric water vapor climatology and trends over North America: 1973–93, *J. Climate*, 9,
725 3561–3574, [https://doi.org/10.1175/1520-0442\(1996\)009<3561:TWVCAT>2.0.CO;2](https://doi.org/10.1175/1520-0442(1996)009<3561:TWVCAT>2.0.CO;2). 1996.

726 Saastamoinen, J.: Atmospheric correction for the troposphere and stratosphere in radio ranging satellites, in: The Use of
727 Artificial Satellites for Geodesy, *Geophys. Monogr. Ser.*, 15, 247–251, AGU, Washington, D.C.,
728 <https://doi.org/10.1029/GM015p0247>, 1972.

729 Soden, B. J. and Lanzante, J. R.: An assessment of satellite and radiosonde climatologies of upper-tropospheric water vapor,
730 *J. Climate*, 9, 1235–1250, [https://doi.org/10.1175/1520-0442\(1996\)009<1235:AAOSAR>2.0.CO;2](https://doi.org/10.1175/1520-0442(1996)009<1235:AAOSAR>2.0.CO;2), 1996.

731 Steinke, S., Ebell, K., Löhnert, U., Bozzo, A., Crewell, S., and Turner, D. D.: Assessment of small-scale integrated water
732 vapour variability during HOPE, *Atmos. Chem. Phys.*, 15, 2675–2692, <https://doi.org/10.5194/acp-15-2675-2015>, 2015.

733 Thayer, G. D.: An improved equation for the radio refractive index of air, *Radio Sci.*, 9, 803–807,
734 <https://doi.org/10.1029/RS009i010p00803>, 1974.

735 Trenberth, K. E., Fasullo, J., and Smith, L.: Trends and variability in column-integrated atmospheric water vapor, *Clim.*
736 *Dynam.*, 24, 741–758, <https://doi.org/10.1007/s00382-005-0017-4>, 2005.

737 Van Malderen, R., Brenot, H., Pottiaux, E., Beirle, S., Hermans, C., De Mazière, M., ... and Bruyninx, C.: A multi-site
738 intercomparison of integrated water vapour observations for climate change analysis, *Atmos. Meas. Tech.*, 7, 2487–2512,
739 <https://doi.org/10.5194/amt-7-2487-2014>, 2014.

740 Van Malderen, R., Pottiaux, E., Stankunavicius, G., Beirle, S., Wagner, T., Brenot, H., Bruyninx, C., and Jones, J.: Global
741 Spatiotemporal Variability of Integrated Water Vapor Derived from GPS, GOME/SCIAMACHY and ERA-Interim: Annual
742 Cycle, Frequency Distribution and Linear Trends. *Remote Sens.*, 14, 1050, <https://doi.org/10.3390/rs14041050>, 2022.

743 Van Baelen, J., Aubagnac, J.P. and Dabas, A.: Comparison of near–real time estimates of integrated water vapor derived with
744 GPS, radiosondes, and microwave radiometer. *Journal of Atmospheric and Oceanic Technology*, 22(2), pp.201-210, 2005.

745 Vaquero-Martínez, J., Antón, M., Ortiz de Galisteo, J. P., Cachorro, V. E., Wang, H., González-Abad, G., ... and Costa, M. J.:
746 Inter-comparison of integrated water vapor from ground-based GPS and satellite remote sensing at Mediterranean sites, IEEE
747 J. Sel. Top. Appl., 11, 1718–1728, <https://doi.org/10.1109/JSTARS.2018.2812804>, 2018.

748 Ware, R., Cimini, D., Herzegh, P., Marzano, F., Vivekanandan, J. and Westwater, E.: Ground-based microwave radiometer
749 measurements during precipitation. In *8th Specialist Meeting on Microwave Radiometry* (pp. 24-27), 2004.

750 Wang, Junhong, Liangying Zhang, and Aiguo Dai. "Global estimates of water-vapor-weighted mean temperature of the
751 atmosphere for GPS applications." *Journal of Geophysical Research: Atmospheres* 110, no. D21. doi:10.1029/2005JD006215.
752 2005.

753 Yao, Y., Zhang, B., Yue, S., Xu, C., and Peng, W.: Analysis of the global Tm-Ts correlation and establishment of the latitude-
754 related linear model, Chin. Sci. Bull., 59, 2340–2347, <https://doi.org/10.1007/s11434-014-0275-9>, 2014.

755 Ziskin Ziv, S., Yair, Y., Alpert, P., Uzan, L., and Reuveni, Y.: The diurnal variability of precipitable water vapor derived from
756 GPS tropospheric path delays over the Eastern Mediterranean, Atmos. Res., 249, 105307,
757 <https://doi.org/10.1016/j.atmosres.2020.105307>, 2021.

758 Ziskin Ziv, S., Alpert, P., and Reuveni, Y.: Long-term variability and trends of precipitable water vapour derived from GPS
759 tropospheric path delays over the Eastern Mediterranean, Int. J. Climatol., 41, 6433–6454, <https://doi.org/10.1002/joc.7205>,
760 2021.

761 Zittis, G., Hadjinicolaou, P., Klangidou, M., et al.: A multi-model, multi-scenario, and multi-domain analysis of regional
762 climate projections for the Mediterranean, Reg. Environ. Change, 19, 2621–2635, <https://doi.org/10.1007/s10113-019-01565->
763 w, 2019.